Asymmetric Tensor Analysis for Flow Visualization

Eugene Zhang, Harry Yeh, Zhongzang Lin, and Robert S. Laramee

***Abstract*— The gradient of a velocity vector field is an asymmetric tensor field which can provide critical insight into the vector field that is difficult to infer from traditional trajectory-based vector field visualization techniques. We describe the structures in the eigenvalue and eigenvector fields of the gradient tensor and how these structures can be used to infer the behaviors of the velocity field that can represent either a 2D compressible flow or the projection of a 3D compressible or incompressible flow onto a two-dimensional manifold.**

The structure in the eigenvalue field is illustrated using the *eigenvalue manifold*, which enables novel visualizations that depict the relative strengths among the physical components in the vector field, such as isotropic scaling, rotation, and anisotropic stretching.

Our eigenvector analysis is based on the concept of the *eigenvector manifold*, which affords additional insight on 2D asymmetric tensors fields beyond previous analyses. Our results include a simple and intuitive geometric realization of the *dual-eigenvectors*, a novel symmetric discriminant that measures the signed distance of a tensor from being symmetric, the classification of degenerate (circular) points, and the extension of the *Poincaré-Hopf index theorem* to continuous asymmetric tensor fields defined on closed two-dimensional manifolds. We also extend eigenvectors continuously into the complex domains which we refer to as pseudo-eigenvectors. We make use of evenly-spaced tensor lines following pseudo-eigenvectors to illustrate the local linearization of tensors everywhere inside complex domains simultaneously.

Both eigenvalue manifold and eigenvector manifold are supported by a tensor reparamterization that has physical meaning. This allows us to relate our tensor analysis to physical quantities such as vorticity, deformation, expansion, contraction, which provide physical interpretation of our tensor-driven vector field analysis in the context of fluid mechanics.

To demonstrate the utility of our approach, we have applied our visualization techniques and interpretation to the study of the *Sullivan Vortex* as well as computational fluid dynamics simulation data.

***Index Terms*— Tensor field visualization, flow analysis, asymmetric tensors, topology, surfaces.**

I. Introduction

VECTOR field analysis and visualization are an integral part of a number of applications in the field of aero- and hydro-dynamics. Local fluid motions comprise translation, rotation, expansion, contraction, and stretching. Most existing flow visualization techniques focus on the velocity vector field of the flow and have led to effective illustrations of the translational component. On the other hand, other flow motions may be the center of interest as well. For example, stretching of fluid parcels can be a good indicator for the rate of fluid mixing and energy dissipation, rotation expresses the amount of vorticity, and expansion and contraction are related to change of volume [2], [10], [24], [27]. The non-translational components are directly related to the gradient tensor of the vector field. Consequently, inferring them using traditional vector field visualization methods that use arrows, streamlines, and colors encoding the magnitude of the vector field (Figure 1 (a-c)) is difficult even to the trained fluid dynamics researchers.

The gradient tensor has found application in a wide range of vector field visualization tasks such as fixed point classification and separatrix computation [12], attachment and separation line extraction [17], vortex core identification [28], [16], [25], [26], and periodic orbit detection [4]. However, the use of the gradient tensor in these applications is often limited to point-wise computation and analysis. There has been relatively little work in investigating the structures in the gradient tensors as a tensor field and what information about the vector field can be inferred from these structures. While symmetric tensor fields have been well explored, it is not clear how structures in symmetric tensor fields can be used to reveal structures in asymmetric tensor fields due to the existence of the anti-symmetric components.

Zheng and Pang are the first to study the structures in 2D asymmetric tensor fields [39]. To our knowledge, this is the only work where the focus of the analysis is on asymmetric tensor fields. In their research, Zheng and Pang introduce the concept of *dual-eigenvectors* inside *complex domains* where eigenvalues and eigenvectors are complex. When the tensor field is the gradient of a vector field, Zheng and Pang demonstrate that dual-eigenvectors represent the elongated directions of the local linearization inside complex domains. Consequently, tensor field structures can be visualized using the combination of eigenvectors and dual-eigenvectors.

The work of Zheng and Pang has inspired this study of asymmetric tensor fields. In particular, we address a number questions that have been left unanswered. First, their algorithm for computing the dual-eigenvectors relies on eigenvector computation or singular value decomposition, neither of which provides much geometric intuition. Thus, a natural question is whether a more explicit relationship exists and if so what information about the vector field can be revealed from this relationship. Second, Zheng and Pang define *circular points* for asymmetric tensor fields that are the counterpart of degenerate points in symmetric tensors. While they provide a *circular discriminant* that can be used to detect circular points, it is not clear how to compute the tensor index of circular points,

E. Zhang is an Assistant Professor of the School of Electrical Engineering and Computer Science, Oregon State University, 2111 Kelley Engineering Center, Corvallis, OR 97331. Email: zhange@eecs.oregonstate.edu.

H. Yeh is a Professor in Fluid Mechanics of the School of Civil Engineering, Oregon State University, 220 Owen Hall, Corvallis, OR 97331. Email: harry@engr.orst.edu.

Z. Lin is a Ph.D. student of the School of Electrical Engineering and Computer Science, Oregon State University, 1148 Kelley Engineering Center, Corvallis, OR 97331. Email: lin@eecs.oregonstate.edu.

R. S. Laramee is a Lecturer (Assistant Professor) of the Department of Computer Science, Swansea University, SA2 8PP, Wales, UK. Email: R.S.Laramee@swansea.ac.uk.

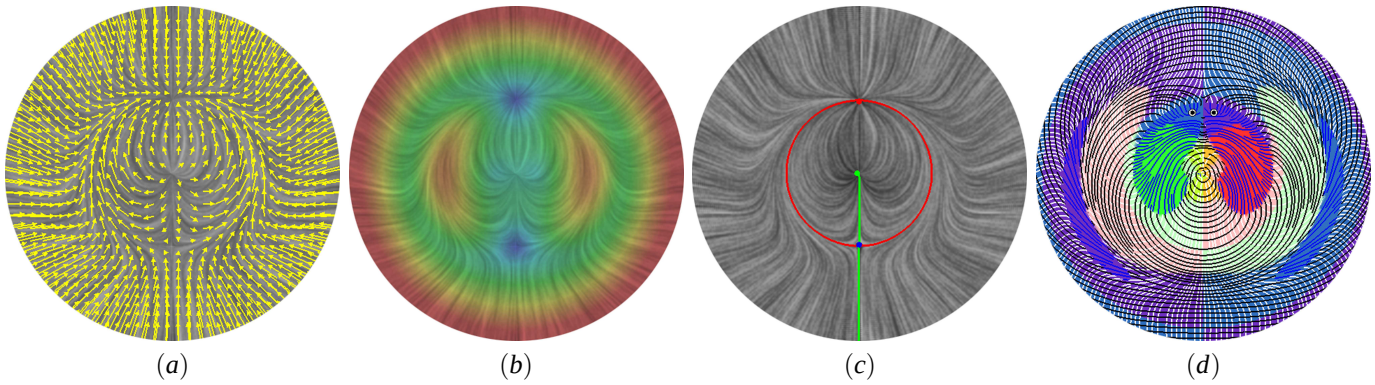

Fig. 1. The gradient tensor of a vector field (d) can provide additional information about the vector field that is difficult to extract from traditional vector field visualization techniques, such as arrow plots (a), trajectories and color coding of vector field magnitude (b), or vector field topology (c) [4]. The colors in (d) indicate the dominant flow motion (without translation) such as isotropic scaling, rotation, and anisotropic stretching. The tensor lines in (d) show the structures in the eigenvectors and dual-eigenvectors of the tensor, which reflect the directions of anisotropic stretching. Notice that it is a challenging task to use vector field visualization techniques (a-c) to provide insight such as locating stretching-dominated regions in the flow and identifying places where the orientations of the stretching change significantly. On the other hand, visualizations based on the gradient tensor such as (d) facilitate the understanding of these important questions. Detailed description for (d) will be discussed in Section IV-B. The flow field shown here is a planar slice of a three-dimensional vector field that is generated by linear superposition of two Sullivan Vortices with opposite orientations [29] (Section V-A).

i.e., circular point classification (wedges, trisectors, etc). Third, eigenvalues are an important aspect of tensor fields. Yet, there is little discussion on the structures of eigenvalues by Zheng and Pang. Finally, the focus of Zheng and Pang is on general asymmetric tensor fields, and there is limited investigation of the physical interpretation of their results in the context of flow analysis.

To address these fundamental issues, we make the following contributions:

1) We introduce the concepts of *eigenvalue manifold* (a hemisphere) and *eigenvector manifold* (a sphere), both of which facilitate tensor analysis (Section IV).
2) With the help of the eigenvector manifold, we extend the theoretical results of Zheng and Pang on eigenvector analysis (Section IV-A) by:
   a) providing an explicit and geometric characterization of the dual-eigenvectors (Section IV-A.1), which enables degenerate point classification (Section IV-A.2),
   b) extending the Poincaré-Hopf theorem to asymmetric tensor fields defined on two-dimensional manifolds (Section IV-A.2),
   c) and introducing pseudo-eigenvectors which we use to illustrate the elliptical flow patterns in the complex domains (Section IV-A.3).
3) We provide eigenvalue analysis based on a Voronoi partition of the eigenvalue manifold (Section IV-B) which allows us to maintain the relative strengths among the three main non-translational flow components: isotropic scaling, rotation, and anisotropic stretching. This partition also demonstrates that direct transitions between certain dominant-to-dominant components are impossible, such as between clockwise and counterclockwise rotations. The transition must go through a dominant flow pattern other than rotation.
4) We present a number of novel vector and tensor field visualization techniques based on our eigenvalue and eigenvector analysis (Sections IV-A and IV-B).
5) Our analysis and visualization techniques can apply to asymmetric tensor fields on two-dimensional manifolds in 3D (Sections V-B and V-C). To our knowledge, this is the first time asymmetric tensor fields on surfaces embedded in 3D are analyzed and visualized.
6) We provide physical interpretation of our analysis in the context of flow visualization (Section V).

The remainder of the paper is organized as follows. We will first review related existing techniques in vector and tensor field visualization and analysis in Section II and provide relevant background on symmetric and asymmetric tensor fields in Section III. Then in Section IV, we describe our analysis and visualization approaches for asymmetric tensor fields defined on two-dimensional manifolds. We provide some physical intuition about our approach and demonstrate the effectiveness of our analysis and visualization by applying them to the Sullivan Vortex as well as cooling jacket and diesel engine simulation applications in Section V. Finally, we summarize our work and discuss some possible future directions in Section VI.

II. Previous Work

There has been extensive work in vector field analysis and flow visualization [20], [21]. However, relatively little work has been done in the area of flow analysis by studying the structures in the gradient tensor, an asymmetric tensor field. In general, previous work is limited to the study of symmetric, second-order tensor fields. Asymmetric tensor fields are usually decomposed into a symmetric tensor field and a rotational vector field and then visualized simultaneously (but as two separate fields). In this section, we review related work in symmetric and asymmetric tensor fields.

A. Symmetric Tensor Field Analysis and Visualization

Symmetric tensor field analysis and visualization has been well researched for both two- and three-dimensions. To refer

to all past work is beyond the scope of this paper. Here we will only refer to the most relevant work.

Delmarcelle and Hesselink [7] provides a comprehensive study on the topology of two-dimensional symmetric tensor fields and define *hyperstreamlines* (also referred to as *tensor lines*), which they use to visualize tensor fields. This research is later extended to analysis in three-dimensions [13], [38], [40] and topological tracking in time-varying symmetric tensor fields [30].

Zheng and Pang provide a high-quality texture-based tensor field visualization technique, which they refer to as *HyperLIC* [37]. This work adapts the idea of *Line Integral Convolution* (*LIC*) of Cabral and Leedom [3] to symmetric tensor fields. Zhang et al. [35] develop a fast and high-quality texture-based tensor field visualization technique, which is a non-trivial adaptation of the *Image-Based Flow Visualization* (*IBFV*) of van Wijk [33]. Hotz et al. [15] present a texture-based method for visualizing 2D symmetric tensor fields. Different constituents of the tensor field corresponding to stress and strain are mapped to visual properties of a texture emphasizing regions of expansion and contraction.

To reduce the noise and small-scale features in the data and therefore enhance the effectiveness of visualization, a symmetric tensor field is often simplified either geometrically through Laplacian smoothing of tensor values [1], [35] or topologically using degenerate point pair cancellation [31], [35] and degenerate point clustering [32].

We also note that the results presented in this paper exhibit some resemblance to those using *Clifford Algebra* [9], [14], [8], in which vector fields are decomposed into different local patterns, e.g., sources, sinks, and shear flows, and then color-coded.

B. Asymmetric Tensor Field Analysis and Visualization

Analysis of asymmetric tensor fields is relatively new in visualization. Zheng and Pang provide analysis on 2D asymmetric tensors [39]. Their analysis includes the partition of the domain into real and complex, defining and use of dual-eigenvectors for the visualization of tensors inside complex domains, incorporation of degenerate curves into tensor field topology, and a circular discriminant that enables the detection of degenerate points (circular points).

In this paper, we extend the analysis of Zheng and Pang by providing an explicit formulation of the dual-eigenvectors, which allows us to perform degenerate point classification and extend the Poincaré-Hopf theorem to two-dimensional asymmetric tensor fields. We also introduce the concepts of pseudo-eigenvectors which can be used to illustrate the elliptical patterns inside complex domains. Such illustration cannot be achieved through the visualization of dual-eigenvectors. Moreover, we provide the analysis on the eigenvalues which we incorporate into visualization. Finally, we provide explicit physical interpretation of our analysis in the context of flow semantics.

III. Background on Tensor Fields

We first review some relevant facts about tensor fields on two-dimensional manifolds. An asymmetric tensor field T for a manifold surface $\mathbf{M}$ is a smooth tensor-valued function that associates with every point $\mathbf{p} \in \mathbf{M}$ a second-order tensor $T(\mathbf{p}) = \begin{pmatrix} T_{11}(\mathbf{p}) & T_{12}(\mathbf{p}) \\ T_{21}(\mathbf{p}) & T_{22}(\mathbf{p}) \end{pmatrix}$ under some local coordinate system in the tangent plane at $\mathbf{p}$. The entries of $T(\mathbf{p})$ depend on the choice of the coordinate system. A tensor $[T_{ij}]$ is *symmetric* if $T_{ij} = T_{ji}$.

A. Symmetric Tensor Fields

A symmetric tensor T can be uniquely decomposed into the sum of its isotropic part D and the (*deviatoric tensor*) A:

$$D + A = \begin{pmatrix} \frac{T_{11}+T22}{2} & 0 \\ 0 & \frac{T_{11}+T22}{2} \end{pmatrix} + \begin{pmatrix} \frac{T_{11}-T_{22}}{2} & T_{12} \\ T_{12} & \frac{T_{22}-T_{11}}{2} \end{pmatrix} \quad (1)$$

T has eigenvalues $\gamma_d \pm \gamma_s$ in which $\gamma_d = \frac{T_{11}+T22}{2}$ and $\gamma_s = \frac{\sqrt{(T_{11}-T_{22})^2+4T_{12}^2}}{2} \geq 0$. Let $E_1(\mathbf{p})$ and $E_2(\mathbf{p})$ be unit eigenvectors that correspond to eigenvalues $\gamma_d + \gamma_s$ and $\gamma_d - \gamma_s$, respectively. E_1 and E_2 are the *major* and *minor* eigenvector fields of T. $T(\mathbf{p})$ is equivalent to two orthogonal eigenvector fields: $E_1(\mathbf{p})$ and $E_2(\mathbf{p})$ when $A(\mathbf{p}) \neq 0$. Delmarcelle and Hesselink [6] suggest visualizing *tensor lines*, which are curves that are tangent to an eigenvector field everywhere along its path.

Different tensor lines can only meet at degenerate points, where $A(\mathbf{p}_0) = 0$ and major and minor eigenvectors are not well-defined. The most basic types of degenerate points are: *wedges* and *trisectors*. Delmarcelle and Hesselink [6] define a *tensor index* for an isolated degenerate point $\mathbf{p}_0$, which must be a multiple of $\frac{1}{2}$ due to the sign ambiguity in tensors. It is $\frac{1}{2}$ for a wedge, $-\frac{1}{2}$ for a trisector, and 0 for a regular point. Delmarcelle shows that the total indices of a tensor field with only isolated degenerated points is related to the topology of the underlying surface [5]. Let $\mathbf{M}$ be a closed orientable manifold with an Euler characteristic $\chi(\mathbf{M})$, and let T be a continuous symmetric tensor field with only isolated degenerate points $\{\mathbf{p}_i : 1 \leq i \leq N\}$. Denote the tensor index of $\mathbf{p}_i$ as $I(\mathbf{p}_i, T)$. Then:

$$\sum_{i=1}^{N} I(\mathbf{p}_i, T) = \chi(\mathbf{M}) \quad (2)$$

In this paper, we will adapt the classification of degenerate points of symmetric tensor fields to asymmetric tensor fields.

B. Asymmetric Tensor Fields

An asymmetric tensor differs from a symmetric one in many aspects, the most significant of which is perhaps that an asymmetric tensor can have complex eigenvalues for which no real-valued eigenvectors exist. Given an asymmetric tensor field T, the domain of T can be partitioned into *real domains* (real eigenvalues λ_i where $\lambda_1 \neq \lambda_2$), *degenerate curves* (real eigenvalues λ_i where $\lambda_1 = \lambda_2$), and *complex domains* (complex eigenvalues). Degenerate curves form the boundary between the real domains and complex domains.

In the complex domains where no real eigenvectors exist, Zheng and Pang [39] introduce the concept of *dual-eigenvectors* which are real-valued vectors and can be used to

describe the elongated directions of the elliptical patterns when the asymmetric tensor field is the gradient of a vector field. The dual-eigenvectors in the real domains are the bisectors between the major and minor eigenvectors. The following equations characterize the relationship between the dual-eigenvectors J_1 (major) and J_2 (minor) and the eigenvectors E_1 (major) and E_2 (minor) in the real domains:

$$E_1 = \sqrt{\mu_1}J_1 + \sqrt{\mu_2}J_2, \quad E_2 = \sqrt{\mu_1}J_1 - \sqrt{\mu_2}J_2 \tag{3}$$

as well as in the complex domains:

$$E_1 = \sqrt{\mu_1}J_1 + i\sqrt{\mu_2}J_2, \quad E_2 = \sqrt{\mu_1}J_1 - i\sqrt{\mu_2}J_2 \tag{4}$$

where μ_1 and μ_2 are the singular values in the singular value decomposition. Furthermore, the following fields:

$$V_i(\mathbf{p}) = \begin{cases} E_i(\mathbf{p}) & T(\mathbf{p}) \text{ in the real domain} \\ J_1(\mathbf{p}) & T(\mathbf{p}) \text{ in the complex domain} \end{cases} \tag{5}$$

$i = 1,2$ are continuous across degenerate curves. Either field can be used to visualize the asymmetric tensor field.

Dual-eigenvectors are undefined at *degenerate points*, where the *circular discriminant*:

$$\Delta_2 = (T_{11} - T_{22})^2 + (T_{12} + T_{21})^2 \tag{6}$$

achieves a value of zero. Degenerate points represent locations where flow patterns are purely circular, and they only occur inside complex domains. They are also referred to as *circular points* [39], and together with degenerate curves they form the *asymmetric tensor field topology*.

In this paper, we extend the aforementioned analysis of Zheng and Pang [39] in several aspects that include a geometric interpretation of the dual-eigenvectors (Section IV-A.1), the classification of degenerate points and the extension of the Poincaré-Hopf theorem from symmetric tensor fields (Equation 2) to asymmetric tensor fields (Section IV-A.2), the introduction and use of *pseudo-eigenvectors* for the visualization of tensor structures inside complex domains (Section IV-A.3), and the incorporation of eigenvalue analysis (Section IV-B).

IV. Asymmetric Tensor Field Analysis and Visualization

Our asymmetric tensor field analysis starts with a parameterization for the set of 2×2 tensors.

It is well known that any second-order tensor can be uniquely decomposed into the sum of its symmetric and anti-symmetric components, which measure the impacts of scaling and rotation caused by the tensor, respectively. Another popular decomposition removes the trace component from a symmetric tensor which corresponds to isotropic scaling (Equation 1). The remaining constituent, the *deviatoric tensor*, has a zero trace and measures the anisotropy in the original tensor. We combine both decompositions to obtain the following unified parameterization of the space of 2×2 tensors:

$$T = \gamma_d \begin{pmatrix} 1 & 0 \\ 0 & 1 \end{pmatrix} + \gamma_r \begin{pmatrix} 0 & -1 \\ 1 & 0 \end{pmatrix} + \gamma_s \begin{pmatrix} \cos\theta & \sin\theta \\ \sin\theta & -\cos\theta \end{pmatrix} \tag{7}$$

where $\gamma_d = \frac{T_{11}+T_{22}}{2}$, $\gamma_r = \frac{T_{21}-T_{12}}{2}$, $\gamma_s = \frac{\sqrt{(T_{11}-T_{22})^2+(T_{12}+T_{21})^2}}{2}$ are the *strengths* of isotropic scaling, rotation, and anisotropic stretching, respectively. Note that $\gamma_s \geq 0$ while γ_r and γ_d can be any real number. $\theta \in [0, 2\pi)$ is the angular component of the vector $\begin{pmatrix} T_{11}-T_{22} \\ T_{12}+T_{21} \end{pmatrix}$, which encodes the orientation of the stretching.

In this paper, we focus on how the relative strengths of the three components effect the eigenvalues and eigenvectors in the tensor. Given our goals, it suffices to study *unit tensors*, i.e., $\gamma_d^2 + \gamma_r^2 + \gamma_s^2 = 1$.

The space of unit tensors is a three-dimensional manifold, for which direct visualization is formidable. Fortunately, the eigenvalues of a tensor only depend on γ_d, γ_r, and γ_s, while the eigenvectors depend on γ_r, γ_s, and θ. Therefore, we define the *eigenvalue manifold* $\mathbf{M}_\lambda$ as:

$$\{(\gamma_d, \gamma_r, \gamma_s) | \gamma_d^2 + \gamma_r^2 + \gamma_s^2 = 1 \text{ and } \gamma_s \geq 0\} \tag{8}$$

and the *eigenvector manifold* $\mathbf{M}_v$ as:

$$\{(\gamma_r, \gamma_s, \theta) | \gamma_r^2 + \gamma_s^2 = 1 \text{ and } \gamma_s \geq 0 \text{ and } 0 \leq \theta < 2\pi\}. \tag{9}$$

Both $\mathbf{M}_\lambda$ and $\mathbf{M}_v$ are two-dimensional, and their structures can be understood in a rather intuitive fashion. A second-order tensor field $T(\mathbf{p})$ defined on a two-dimensional manifold $\mathbf{M}$ introduces the following *continuous* maps:

$$\zeta_T : \mathbf{M} \to \mathbf{M}_\lambda, \quad \eta_T : \mathbf{M} \to \mathbf{M}_v, \tag{10}$$

In the next two sections, we describe the analysis of $\mathbf{M}_\lambda$ and $\mathbf{M}_v$.

A. Eigenvector Manifold

The analysis on eigenvectors and dual-eigenvectors by Zheng and Pang [39] can be largely summarized by Equations 3-6. The eigenvector manifold presented here not only allows us to provide more geometric (intuitive) reconstruction of their results, but also leads to novel analysis that includes the classification of degenerate points, extension of the Poincaré-Hopf theorem to two-dimensional asymmetric tensor fields, and the definition of pseudo-eigenvectors which we use to visualize tensor structures inside the complex domains. We begin with the definition of the eigenvector manifold.

The eigenvectors of an asymmetric tensor expressed in the form of Equation 7 only depend on γ_r, γ_s, and θ. Given that the tensor magnitude and the isotropic scaling component do not affect the behaviors of eigenvectors, we will only need to consider unit traceless tensors, i.e., $\gamma_d = 0$ and $\gamma_r^2 + \gamma_s^2 = 1$. They have the following form:

$$T(\theta, \varphi) = \sin\varphi \begin{pmatrix} 0 & -1 \\ 1 & 0 \end{pmatrix} + \cos\varphi \begin{pmatrix} \cos\theta & \sin\theta \\ \sin\theta & -\cos\theta \end{pmatrix} \tag{11}$$

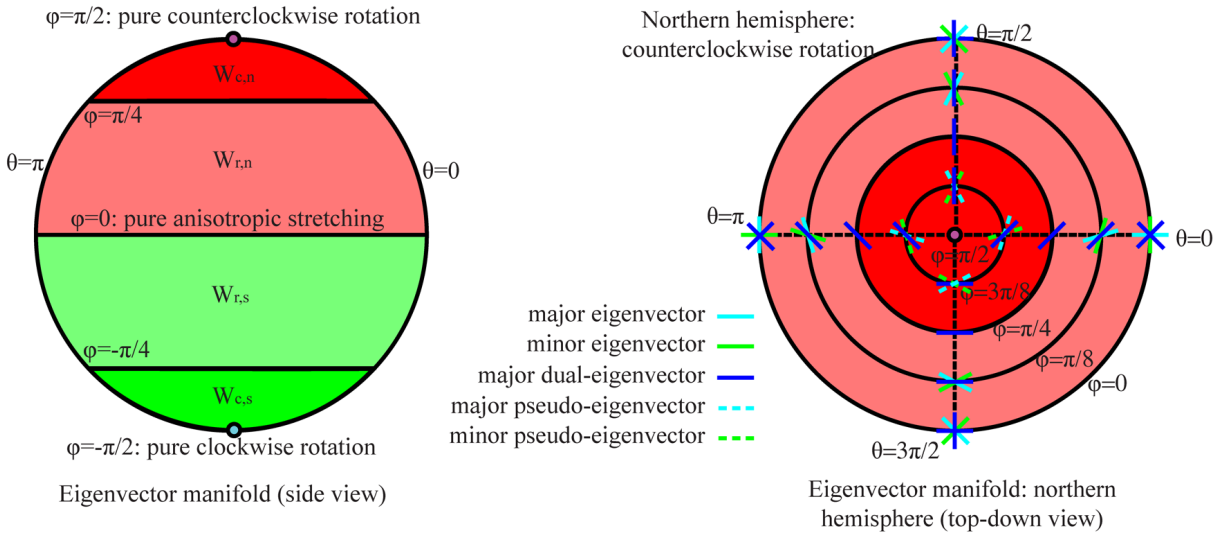

Fig. 2. The eigenvector manifold (left) is partitioned into real domains in the northern hemisphere ($W_{r,n}$) and the southern hemisphere ($W_{r,s}$) as well as complex domains in these hemispheres ($W_{c,n}$ and $W_{c,s}$). The orientation of the rotational component is counterclockwise in the northern hemisphere and clockwise in the southern hemisphere. The equator represents pure symmetric tensors, while the poles represent pure rotations. Along any longitude, (e.g., $\theta = 0$ (right)), and starting from the intersection with the equator and going north (right), the major dual-eigenvectors (blue lines) remain constant. In the real domains, i.e., $0 \leq \varphi < \frac{\pi}{4}$, the angle between the major eigenvectors (solid cyan lines) and the minor eigenvectors (solid green lines) monotonically decreases to 0. The angle is exactly 0 when the magnitude of the stretching constituent equals that of the rotational part. Inside the complex domains where major and minor eigenvectors are not real, pseudo-eigenvectors (cyan and green dashed lines, details in Definition 4.6) are used for visualization purposes. The major and minor pseudo-eigenvectors at φ ($\frac{\pi}{4} < \varphi < \frac{\pi}{2}$) are defined to be the same as the minor and major eigenvectors for $\frac{\pi}{2} - \varphi$ along the same longitude. Traveling south of the equator towards the south pole, the behaviors of the eigenvectors and pseudo-eigenvectors are similar except they rotate in the opposite direction. At the equator, there are two bisectors, i.e., major and minor dual-eigenvectors cannot be distinguished. We consider the equator a bifurcation point and therefore part of tensor field topology. On a different longitude, the same pattern repeats except the eigenvectors, dual-eigenvectors, and pseudo-eigenvectors are rotated by a constant angle. Different longitudes correspond to different constant angles.

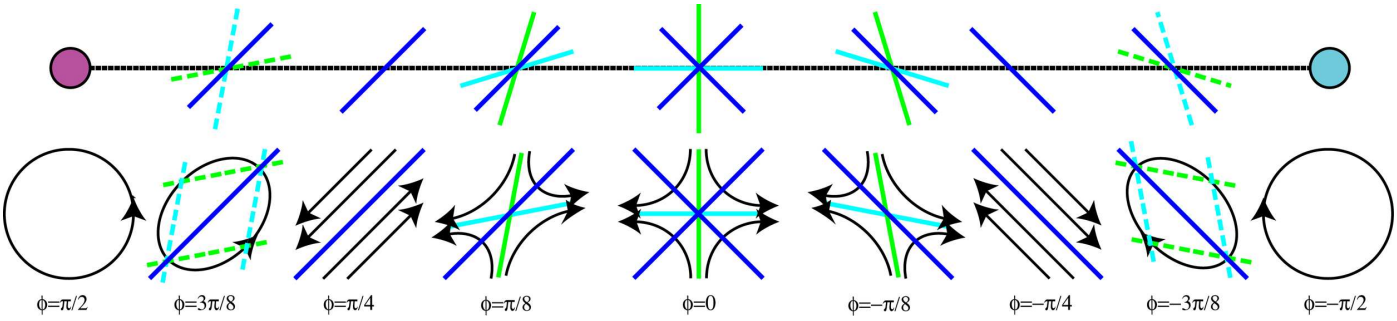

Fig. 3. Example vector fields whose gradient tensors correspond to points along the longitude $\theta = 0$ (Figure 2 (right)).

in which $\varphi = \arctan(\frac{\gamma_r}{\gamma_s}) \in [-\frac{\pi}{2}, \frac{\pi}{2}]$. Consequently, the set of unit traceless 2×2 tensors can be represented by a unit sphere which we refer to as the *eigenvector manifold* (Figure 2 (left)). The following observation provides some intuition about the eigenvector manifold.

Theorem 4.1: Given two tensors $T_i = T(\theta_i, \varphi)$ $(i = 1, 2)$ on the same latitude $-\frac{\pi}{2} < \varphi < \frac{\pi}{2}$, let $N = \begin{pmatrix} \cos\delta & -\sin\delta \\ \sin\delta & \cos\delta \end{pmatrix}$ with $\delta = \frac{\theta_2 - \theta_1}{2}$. Then any eigenvector or dual-eigenvector $\overrightarrow{w_2}$ of T_2 can be written as $N\overrightarrow{w_1}$ where $\overrightarrow{w_1}$ is an eigenvector or dual-eigenvector of T_1, respectively.

The proofs of this theorem and the theorems thereafter are provided in the Appendix.

Theorem 4.1 states that as one travels along a latitude in the eigenvector manifold, the eigenvectors and dual-eigenvectors are rotated at the same rate. This suggests that the fundamental behaviors of eigenvectors and dual-eigenvectors are dependent on φ only. In contrast, θ only impacts the directions of the eigenvectors and dual-eigenvectors, but not their relatively positions (Figure 2, right).

Next, we will make use of the eigenvector manifold to provide a geometric construction of the dual-eigenvectors (Section IV-A.1), classify degenerate points and extend the Poincaré-Hopf theorem to asymmetric tensor fields (Section IV-A.2), and introduce the pseudo-eigenvectors which we use to illustrate tensor structures in the complex domains (Section IV-A.3).

1) Geometric Construction of Dual-Eigenvectors: Theorem 4.1 allows us to focus on the behaviors of eigenvectors and dual-eigenvectors along the longitude where $\theta = 0$, for which Equation 11 reduces to:

$$T = \begin{pmatrix} \cos\varphi & -\sin\varphi \\ \sin\varphi & -\cos\varphi \end{pmatrix} \tag{12}$$

The tensors have zero, one, or two real eigenvalues when $\cos 2\varphi < 0$, $= 0$, or > 0, respectively. Consequently, the tensor is referred to as being *in the complex domain*, *on a degenerate curve*, or *in the real domain* [39]. Notice that the tensor is on a degenerate curve if and only if $\varphi = \pm\frac{\pi}{4}$.

In the complex domains, it is straightforward to verify that $\begin{pmatrix}1\\1\end{pmatrix}$ and $\begin{pmatrix}1\\-1\end{pmatrix}$ are the dual-eigenvectors except when $\varphi = \pm\frac{\pi}{2}$, i.e., degenerate points. In the real domains, the eigenvalues are $\pm\sqrt{cos2\varphi}$. A major eigenvector is:

$$\begin{pmatrix}\sqrt{\sin(\varphi+\frac{\pi}{4})}+\sqrt{\cos(\varphi+\frac{\pi}{4})}\\ \sqrt{\sin(\varphi+\frac{\pi}{4})}-\sqrt{\cos(\varphi+\frac{\pi}{4})}\end{pmatrix} \tag{13}$$

and a minor eigenvector is:

$$\begin{pmatrix}\sqrt{\sin(\varphi+\frac{\pi}{4})}-\sqrt{\cos(\varphi+\frac{\pi}{4})}\\ \sqrt{\sin(\varphi+\frac{\pi}{4})}+\sqrt{\cos(\varphi+\frac{\pi}{4})}\end{pmatrix} \tag{14}$$

The bisectors between them are lines $X = Y$ and $X = -Y$ where X and Y are the axes of the coordinate systems in the tangent plane at each point. That is, the dual-eigenvectors in the real domains are also $\begin{pmatrix}1\\1\end{pmatrix}$ and $\begin{pmatrix}1\\-1\end{pmatrix}$. Combined with the dual-eigenvector derivation in the complex domains, it is clear that the dual-eigenvectors remain the same for any $\varphi \in (-\frac{\pi}{2}, \frac{\pi}{2})$. This is significant as it implies that the dual-eigenvectors depend primarily on the symmetric component of a tensor field.

The anti-symmetric (rotational) component impact the dual-eigenvectors in the following way. In the northern hemisphere where $\gamma_r = \sin\varphi > 0$, a major dual-eigenvector is $\begin{pmatrix}1\\1\end{pmatrix}$, and a minor dual-eigenvector is $\begin{pmatrix}1\\-1\end{pmatrix}$. In the southern hemisphere ($\gamma_r = \sin\varphi < 0$), the values of the dual-eigenvectors are swapped. Consequently, the major dual-eigenvector field J_1 is discontinuous across curves where $\varphi = 0$, which correspond to pure symmetric tensors (Equation 11) that form the boundaries between regions of counterclockwise rotations and regions of clockwise rotations.

With the help of Theorem 4.1, the above discussion can be formulated into the following.

Theorem 4.2: The major and minor dual-eigenvectors of a tensor $T(\theta,\varphi)$ are respectively the major and minor eigenvectors of the following symmetric tensor:

$$P_T = \frac{\gamma_r}{|\gamma_r|}\gamma_s \begin{pmatrix}\cos(\theta+\frac{\pi}{2}) & \sin(\theta+\frac{\pi}{2})\\ \sin(\theta+\frac{\pi}{2}) & -\cos(\theta+\frac{\pi}{2})\end{pmatrix} \tag{15}$$

wherever P_T is non-degenerate, i.e., $\gamma_r = \cos\varphi \neq 0$ and $\gamma_s = \sin\varphi \neq 0$.

This inspires us to incorporate places corresponding to $\varphi = 0$ into tensor field topology in addition to $\varphi = \pm\frac{\pi}{4}$ (degenerate curves) and $\varphi = \pm\frac{\pi}{2}$ (degenerate points). Symmetric tensors and degenerate curves divide the eigenvector manifold $\mathbf{M}_v$ into four regions: (1) real domains in the northern hemisphere ($W_{r,n}$), (2) real domains in the southern hemisphere ($W_{r,s}$), (3) complex domains in the northern hemisphere ($W_{c,n}$), and (4) complex domains in the southern hemisphere ($W_{c,s}$). Figure 2 (left) illustrates this partition.

Notice that φ measures the *signed* spherical distance of a unit traceless tensor to pure symmetric tensors (the equator). For example, the north pole has a positive distance and the south pole has a negative distance. In contrast, the circular discriminant Δ_2 (Equation 6) satisfies $\Delta_2 = 4\gamma_s$, which implies that Δ_2 does not make such a distinction between the two hemispheres. Therefore, we advocate the use of φ as a measure for the degree of being symmetric of an asymmetric tensor.

2) Degenerate Point Classification: Next, we discuss the degenerate points where dual-eigenvectors are undefined, i.e., circular points. We provide the following definition:

Definition 4.3: Given a continuous asymmetric tensor field T defined a two-dimensional manifold $\mathbf{M}$, let Ω be a small circle around $\mathbf{p}_0 \in \mathbf{M}$ such that Ω contains no additional degenerate points and it encloses only one degenerate point, $\mathbf{p}_0$. Starting from a point on Ω and travelling counterclockwise along Ω, the major dual-eigenvector field (after normalization) covers the unit circle S^1 a number of times. This number is said to be the tensor index of $\mathbf{p}_0$ with respect to T, and is denoted by $I(\mathbf{p}_0, T)$.

We now return to the discussion on degenerate points, which correspond to the poles ($\varphi = \pm\frac{\pi}{2}$), i.e., $\gamma_s = 0$. The relationship between the dual-eigenvectors of an asymmetric tensor $T(\theta,\varphi)$ and the corresponding symmetric tensor P_T described in Equation 15 leads to the following theorem:

Theorem 4.4: Let T be a continuous asymmetric tensor field defined on a two-dimensional manifold $\mathbf{M}$ satisfying $\gamma_r^2 + \gamma_s^2 > 0$ everywhere in $\mathbf{M}$. Let S_T be the symmetric component of T which has a finite number of degenerate points $K = \{\mathbf{p}_i : 1 \le i \le N\}$. Then we have:

1) K is also the set of degenerate points of T.
2) For any degenerate point $\mathbf{p}_i$, $I(\mathbf{p}_i, T) = I(\mathbf{p}_i, S_T)$. In particular, a wedge remains a wedge, and a trisector remains a trisector.

This theorem allows us to not only detect degenerate points, but also classify them based on their tensor indexes (wedges, trisectors, etc) and the hemisphere they dwell on, something not addressed by Zheng and Pang's analysis [39]. Furthermore, this theorem leads directly to the extension of the well-known *Poincaré-Hopf theorem* for vector fields to asymmetric tensor fields as follows.

Theorem 4.5: Let $\mathbf{M}$ be a closed orientable two-dimensional manifold with an Euler characteristic $\chi(\mathbf{M})$, and let T be a continuous asymmetric tensor field with only isolated degenerate points $\{\mathbf{p}_i : 1 \le i \le N\}$. Then:

$$\sum_{i=1}^{N} I(\mathbf{p}_i, T) = \chi(\mathbf{M}) \tag{16}$$

The eigenvector manifold also provides hints that degenerate points occurring at opposite poles have different rotational orientations. In fact, any tensor line connecting a degenerate point pair inside different hemispheres necessarily crosses the equator (pure symmetric tensors) an odd number of times. In contrast, when the degenerate point pair is in the same hemisphere, any connecting tensor line will cross the equator an even number of times or remain in the same hemisphere (zero crossing).

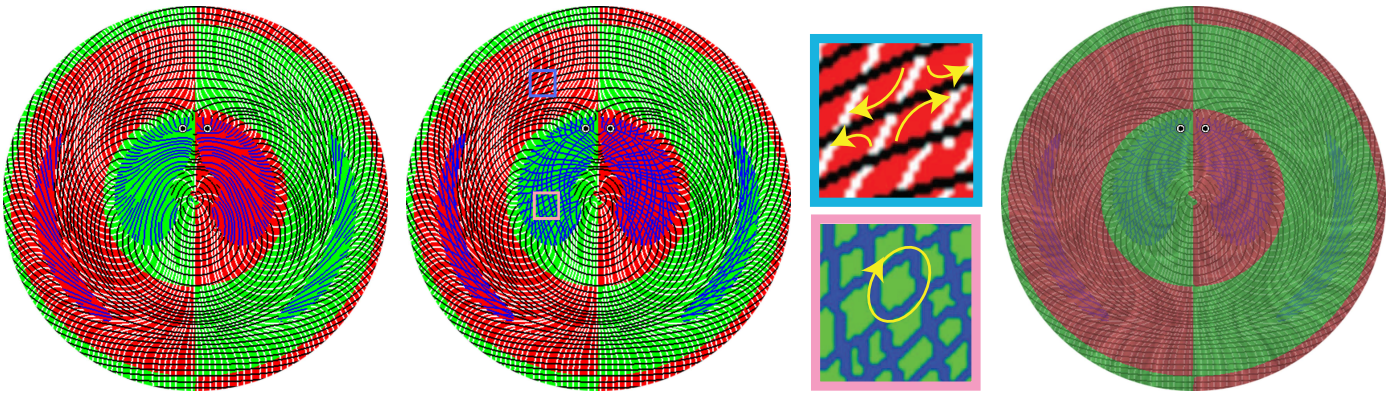

(a) (b) (b′) (c)

Fig. 4. Three tensor line-based techniques in visualizing the eigenvectors of the vector field shown in Figure 1. In (a), the regions with a single family of tensor lines are the complex domains and the regions with two families of tensor lines are the real domains. Red indicates a counterclockwise rotational component while green suggests a clockwise one. The major and minor eigenvectors (real domains) are colored black and white, respectively. The blue tensor lines inside the complex domains follow the major dual-eigenvectors. In (b), dual-eigenvectors are replaced by pseudo-eigenvectors (blue) inside complex domains. The image in (c) is obtained from (b) by blending it with a texture-based visualization of the vector field. In (b'), the physical meanings of eigenvectors (top) and pseudo-eigenvectors (bottom) are annotated.

3) Pseudo-Eigenvectors: We conclude our analysis with the introduction of pseudo-eigenvectors, which like dual-eigenvectors are continuous extensions of eigenvectors into the complex domains. Unlike dual-eigenvectors, however, pseudo-eigenvectors are not mutually perpendicular. Recall that in the complex domains, flow patterns without translations and isotropic scalings are ellipses, whose elongated directions are represented by the major and minor dual-eigenvectors [39]. Unfortunately, the elliptical patterns cannot be demonstrated by drawing tensor lines following the major and minor dual-eigenvectors since they are always mutually perpendicular. To remedy this, we observe that an ellipse can be inferred from the smallest enclosing diamond whose diagonals represent the major and minor axes of the ellipse (Figure 4 (b'): bottom). Given two families of evenly-spaced lines of the same density d intersecting at an angle $\alpha = f(\theta)$, any ellipse can be represented. Our question then is: given a tensor $T(\theta,\varphi)$ where $\frac{\pi}{4} < |\varphi| < \frac{\pi}{2}$, how do we decide the directions of the two families of lines? This leads to the following definitions:

Definition 4.6: Given a tensor $T = T(\theta,\varphi)$, the *major pseudo-eigenvector* of T is defined to be the *minor* eigenvector of the tensor $T(\theta,\frac{\pi}{2}-\varphi)$ when $\varphi > \frac{\pi}{4}$ and $T(\theta,-\frac{\pi}{2}-\varphi)$ when $\varphi < -\frac{\pi}{4}$. Similarly, the *minor pseudo-eigenvector* of T is defined to be the *major* eigenvector of the same tensors under these conditions.

It is straightforward to verify that evenly-spaced lines following the major and minor pseudo-eigenvectors produce diamonds whose smallest enclosing ellipses represent the flow patterns corresponding to T in the complex domains (Figure 3: $\varphi = \pm\frac{3\pi}{8}$). Notice that the definitions of the major and minor pseudo-eigenvectors can be swapped as evenly-spaced lines following either definition produce the same diamonds. Because of this, we assign the same color (blue) to both pseudo-eigenvector fields in our visualization techniques in which they are used (Figure 4 (b-c)).

Both major and minor pseudo-eigenvector fields P_i $(i = 1,2)$ in the complex domains are continuous with respect to the major and minor eigenvector fields E_i $(i = 1,2)$ in the real domains across degenerate curves. Thus we define the *major and minor augmented eigenvector fields* A_i $(i = 1,2)$ as:

$$A_i(\mathbf{p}) = \begin{cases} E_i(\mathbf{p}) & T(\mathbf{p}) \text{ in the real domain} \\ P_i(\mathbf{p}) & T(\mathbf{p}) \text{ in the complex domain} \end{cases} \quad (17)$$

The major and minor pseudo-eigenvectors are undefined at degenerate points, i.e., $\varphi = \pm\frac{\pi}{2}$. In fact, the set of degenerate points of either pseudo-eigenvector field matches that of the major dual-eigenvector field (number, location, tensor index), thus respecting the adapted Poincaré-Hopf theorem for asymmetric tensor fields (Theorem 4.5). The orientations of tensor patterns in the pseudo-eigenvector fields near degenerate points are obtained by rotating patterns in the major dual-eigenvector field in the same regions by $\frac{\pi}{4}$ either counterclockwise ($\varphi > 0$) or clockwise ($\varphi < 0$).

4) Visualizations: In Figure 4, we apply three visualization techniques based on eigenvector analysis to the vector field shown in Figure 1. In addition to the option of visualizing eigenvectors in the real domains and major dual-eigenvectors in complex domain (Figure 4 (a)), pseudo-eigenvectors provide an alternative (Figure 4 (b)). In these images, the background colors are either red (counterclockwise rotation) or green (clockwise rotation). Tensor lines following the major and minor eigenvector fields are colored in black and white, respectively. Tensor lines according to the dual-eigenvector field (a) and pseudo-eigenvector fields (b) are colored in blue, which makes it easy to distinguish between real and complex domains. Degenerate points are highlighted as either black (wedges) or white (trisectors) disks. Note that it is easy to see the topology of tensor fields (degenerate points, degenerate curves, purely symmetric tensors) in these visualization techniques. Figure 4 (c) overlays the eigenvector visualization in (b) onto texture-based visualization of the vector field. It is evident that flow directions do not align with the eigenvector or pseudo-eigenvector directions. Furthermore, as expected the fixed points in the vector field and degenerate points in the tensor field appear in different locations.

B. Eigenvalue Manifold

We now describe our analysis on the eigenvalues of 2×2 tensors, which have the following forms:

$$\lambda_{1,2} = \begin{cases} \gamma_d \pm \sqrt{\gamma_s^2 - \gamma_r^2} & \text{if } \gamma_s^2 \geq \gamma_r^2 \\ \gamma_d \pm \boldsymbol{i}\sqrt{\gamma_r^2 - \gamma_s^2} & \text{if } \gamma_s^2 < \gamma_r^2 \end{cases} \tag{18}$$

Recall that γ_d, γ_r, and γ_s represent the (relative) strengths of the isotropic scaling, rotation, and anisotropic stretching components in the tensor field.

To understand the nature of a tensor usually requires the study of γ_d, γ_r, γ_s, or some of their combinations. Since no upper bounds on these quantities necessarily exist, the effectiveness of the visualization techniques can be limited by the ratio between the maximum and minimum values. However, it is often desirable to answer the following questions:

- What are the relative strengths of the three components (γ_d, γ_r, and γ_s) at a point $\mathbf{p}_0$?
- Which of these components is dominant at $\mathbf{p}_0$?

Both questions are more concerned with the relative ratios among γ_d, γ_r, and γ_s rather than their individual values, which makes it possible to focus on unit tensors, i.e., when $\gamma_d^2 + \gamma_r^2 + \gamma_s^2 = 1$ and $\gamma_s \geq 0$. The set of all possible eigenvalue configurations satisfying these conditions can be modeled as a unit hemisphere, which is a compact two-dimensional manifold (Figure 5 upper-left).

There are five special points in the eigenvalue manifold that represent the extremal situations: (1) pure positive scaling ($\gamma_d = 1,\ \gamma_r = \gamma_s = 0$), (2) pure negative scaling ($\gamma_d = -1,\ \gamma_r = \gamma_s = 0$), (3) pure counterclockwise rotation ($\gamma_r = 1,\ \gamma_d = \gamma_s = 0$), (4) pure clockwise rotation ($\gamma_r = -1,\ \gamma_d = \gamma_s = 0$), and (5) pure anisotropic stretching ($\gamma_s = 1,\ \gamma_d = \gamma_r = 0$) (Figure 5 (upper-left)). The Voronoi diagram with respect to these configurations leads to a partition of the eigenvalue manifold into the following types of regions: (1) D^+ (positive scaling dominated), (2) D^- (negative scaling dominated), (3) R^+ (counterclockwise rotation dominated), (4) R^- (clockwise rotation dominated), and (5) S (anisotropic stretching dominated). Here, the distance function is the spherical geodesic distance, i.e., $d(v_1, v_2) = 1 - v_1 \cdot v_2$ for any two points v_1 and v_2 on the eigenvalue manifold. The resulting diagram is illustrated in Figure 5 (upper-middle).

A point $\mathbf{p}_0$ in the domain is said to be a type D^+ point if $T(\mathbf{p}_0)$ is in the Voronoi cell of pure positive scaling, i.e., $\gamma_d(\mathbf{p}_0) > \max(\gamma_s(\mathbf{p}_0), |\gamma_r(\mathbf{p}_0)|)$. A *$D^+$-type region* R is a connected region in which every point is of type D^+. Points and regions corresponding to the other types can be defined in a similar fashion. We define the topology of a tensor field with respect to eigenvalues as the set of points in the domain whose tensor values map to the boundaries between the Voronoi cells in the eigenvalue manifold. The following result is a straightforward derivation from the Voronoi decomposition of the eigenvalue manifold.

Theorem 4.7: Given a continuous asymmetric tensor field T defined on a two-dimensional manifold $\mathbf{M}$, let U_1 and U_2 be an α- and β-type region, respectively, where $\alpha, \beta \in \{D^+, D^-, R^+, R^-, S\}$ are different. Then $\partial U_1 \bigcap \partial U_2 = \emptyset$ if α- and β-types represent regions in the eigenvalue manifold that do not share a common boundary.

As an application of this theorem, we state that a continuous path travelling from an R^+-type region to an R^--type region must intersect with a D^+-, D^--, or S-type region. A similar statement can be made between a D^+- and D^--type region pair. Note these statements can be difficult to verify without the use of eigenvalue manifold.

We propose two visualization techniques. With the first technique, we assign a unique color to each of the five special configurations shown in Figure 5 (upper-middle). Effective color assignment can allow the user to identify the type of primary characteristic at a given point as well as the relative ratios among the three components. We use the scheme shown in Figure 5 (upper-right): pure positive isotropic scaling (yellow), pure negative isotropic scaling (blue), pure counterclockwise rotation (red), pure clockwise rotation (green), and pure anisotropic stretching (white). For any other point $(\gamma_d(x,y), \gamma_r(x,y), \gamma_s(x,y))$, we compute α as the angular component of the vector $(\gamma_d(x,y), \gamma_r(x,y))$ with respect to $(1,0)$ (counterclockwise rotation). The hue of the color is then:

$$\begin{cases} \frac{2}{3}\alpha & \text{if } \quad 0 \leq \alpha < \pi \\ \frac{4}{3}\alpha & \text{if } -\pi \leq \alpha < 0 \end{cases} \tag{19}$$

Notice that angular distortion ensures that the two isotropic scalings and rotations will be assigned opposite colors, respectively. Our color legend is adopted from Ware [34]. The saturation of the color reflects $\gamma_d^2(x,y) + \gamma_r^2(x,y)$, and the value of the color is always one. This ensures that as the amount of anisotropic stretching increases, the color gradually changes to white, which is consistent with our choice of color for representing anisotropic stretching. Figure 6 (a) illustrates this visualization with the vector field shown in Figure 1.

Our second eigenvalue visualization method assigns a unique color to each of the five Voronoi cells in the eigenvalue manifold. Figure 6 (b) shows this visualization technique for the aforementioned vector field.

Notice that the two techniques differ in how they address the transitions between regions of different dominant characteristics. The first method allows for smooth transitions and preserves relative strengths of γ_d, γ_r, and γ_s, which we refer to as the AC (all components) method. The second method explicitly illustrates the boundaries between regions with different dominant behaviors, which we refer to as the DC (dominant component) method. We use both methods in our interpretations of the data sets (Section V). To illustrate the absolute magnitude of the tensor field, we provide a visualization in which the colors represent the magnitude of the gradient tensor, i.e., $\gamma_d^2 + \gamma_r^2 + \gamma_s^2$ (Figure 6 (c)). In this visualization, red indicates high values and blues indicate low values. Notice that this visualization can provide complementary information than either the AC or DC method.

Combining visualizations based on eigenvalue and eigenvector analysis leads to several hybrid techniques. The following provides some insight on the link between eigenvalue analysis and eigenvector analysis.

Theorem 4.8: Given a continuous asymmetric tensor field T defined on a two-dimensional manifold such that $\gamma_d^2 + \gamma_r^2 +$

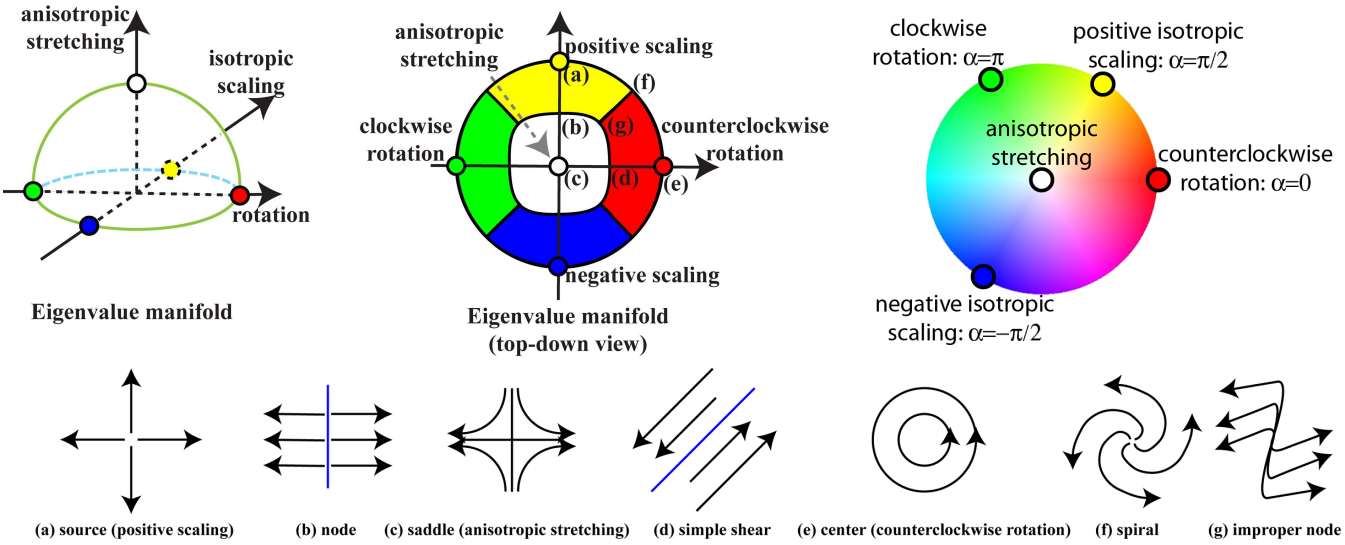

Fig. 5. The eigenvalue manifold of the set of 2×2 tensors. There are five special configurations (top-left: colored dots). The top-middle portion shows a top-down view of the hemisphere along the axis of anisotropic stretching. The hemisphere is decomposed into the Voronoi cells for the five special cases, where the boundary curves are part of tensor field topology. To show the relationship between a vector field and the eigenvalues of the gradient, seven vector fields with constant gradient are shown in the bottom row: (a) $(\gamma_d, \gamma_r, \gamma_s) = (1,0,0)$, (b) $(\frac{\sqrt{2}}{2}, 0, \frac{\sqrt{2}}{2})$, (c) $(0,0,1)$, (d) $(0, \frac{\sqrt{2}}{2}, \frac{\sqrt{2}}{2})$, (e) $(0,1,0)$, (f) $(\frac{\sqrt{2}}{2}, \frac{\sqrt{2}}{2}, 0)$, and (g) $(\frac{\sqrt{3}}{3}, \frac{\sqrt{3}}{3}, \frac{\sqrt{3}}{3})$. Finally, we assign a unique color to every point in the eigenvalue manifold (upper-right). The boundary circle of the eigenvalue manifold is mapped to the loop of the hues. Notice the azimuthal distortion in this map, which is needed in order to assign positive and negative scaling with hues that are perceptually opposite. Similarly we assign opposite hues to distinguish between counterclockwise and clockwise rotations.

Fig. 6. Three visualization techniques on the vector field shown in Figure 1 (Section V-A): (a) eigenvalue visualization based on all components, (b) eigenvalue visualization based on the dominant component, and (c) magnitude (dyadic product) of the velocity gradient tensor. The color scheme for (a) is described in Figure 5 (upper-right). The color scheme for (b) is based on the dominant component in the tensor: positive scaling (green), negative scaling (red), counterclockwise rotation (yellow), clockwise rotation (blue), and anisotropic stretching (white). In (c), red indicates large values and blue indicates small.

$\gamma_s^2 > 0$ everywhere, the following are true:

1) an R^+-type region is contained in $W_{c,n}$ and an R^--type region is contained in $W_{c,s}$,
2) an S-type region is contained in $W_{r,n} \bigcup W_{r,s}$,
3) a D^+-type or D^--type region can have a non-empty intersection with any of the following: $W_{r,n}$, $W_{r,s}$, $W_{c,n}$, and $W_{c,s}$.

Three hybrid visualizations are shown in Figure 7. In (a), the colors are obtained by combining the colors from the eigenvalue visualization (Figure 6 (b)) with the background colors (red or green) from eigenvector visualization (Figure 4 (a)). This results in eight different colors according to Theorem 4.8):

- $C_1 = R^+ \bigcap W_{c,n}$ (red),
- $C_2 = R^- \bigcap W_{c,s}$ (green),
- $C_3 = D^+ \bigcap (W_{c,n} \bigcup W_{r,n})$ (yellow+red),
- $C_4 = D^+ \bigcap (W_{c,s} \bigcup W_{r,s})$ (yellow+green),
- $C_5 = D^- \bigcap (W_{c,n} \bigcup W_{r,n})$ (blue+red),
- $C_6 = D^- \bigcap (W_{c,s} \bigcup W_{r,s})$ (blue+green),
- $C_7 = S \bigcap (W_{c,n} \bigcup W_{r,n})$ (white+red),
- $C_8 = S \bigcap (W_{c,s} \bigcup W_{r,s})$ (white+green),

Furthermore, $C_5 - C_8$ can be in either the real or complex

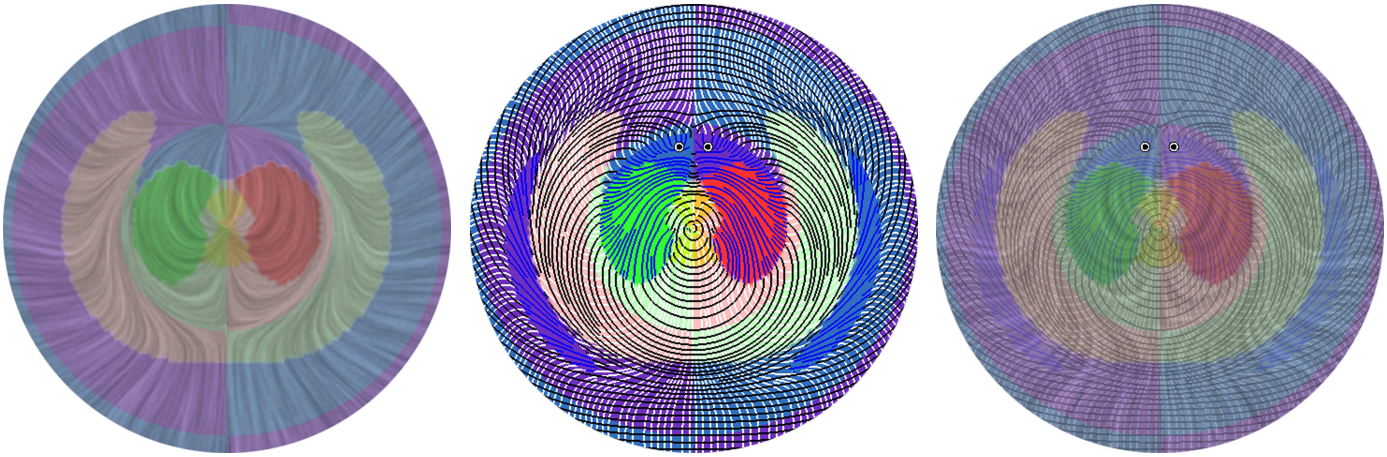

Fig. 7. Example hybrid visualization techniques on the vector field shown in Figure 1: (a) a combination of eigenvalue-based visualization (Figure 6 (b)) with the background color (red and green) from eigenvector-based visualization (Figure 4 (a)), (b) same as (a) except the underlying texture-based vector field visualization is replaced by eigenvectors and major dual-eigenvectors, and (c) a combination of (a) and (b).

domain. This can be distinguished based on the colors of the tensor lines (see Figure 7 (b)): real domains (tensor lines in black and white) and complex domains (tensor lines in blue). Figure 7 (c) is obtained by combining the visualizations in Figure 7 (a) and (b).

C. Computation of Field Parameters

Our system can accept either a tensor field or a vector field. In the latter case, the vector gradient (a tensor) is used as the input. The computational domain is a triangular mesh in either a planar domain or a curved surface. The vector or tensor field is defined at the vertices only. To obtain values at a point on the edge or inside a triangle, we use a piecewise interpolation scheme. On surfaces, we use the scheme of Zhang et al. [36], [35] that ensures vector and tensor field continuity in spite of the discontinuity in the surface normal.

Given a tensor field T, we first perform the following computation for every vertex.

- Repamaterization, in which we compute γ_d, γ_r, γ_s, and θ.
- Normalization, in which we scale γ_d, γ_r, and γ_s to ensure $\gamma_d^2+\gamma_r^2+\gamma_d^s=1$.
- Eigenvector analysis, in which we extract the eigenvectors, dual-eigenvectors, and pseudo-eigenvectors at each vertex.

Next, we extract the topology of the tensor field with respect to the eigenvalues. This is done by visiting every edge in the mesh to locate possible intersection points with the boundary curves of the Voronoi cells shown in Figure 5. We then connect the intersection points whenever appropriate.

Finally, we extract tensor topology based on eigenvectors. This includes the detection and classification of degenerate points as well as the extraction of degenerate curves and symmetric tensors.

V. Physical Interpretation and Applications

In this section, we describe the physical interpretation of our asymmetric tensor analysis in the context of fluid flow fields. Let u be the flow velocity. The velocity gradient tensor ∇u consists of all the possible fluid motions except translation and can be decomposed into three terms [2], [27]:

$$\nabla u = \frac{\text{trace}[\nabla u]}{N}\delta_{ij} + \Omega_{ij} + E_{ij} \tag{20}$$

where δ_{ij} is the *Kronecker delta*, N is the dimension of the domain (either 2 or 3), $\frac{\text{trace}[\nabla u]}{N}\delta_{ij}$ represents the volume distortion or expansion and contraction (equivalent to *isotropic scaling* in mathematical terms), and the anti-symmetric tensor $\Omega_{ij}=\frac{1}{2}(\nabla u-(\nabla u)^T)$ represents the averaged rotation of a fluid parcel. Since Ω_{ij} has only three entities when $N=3$, it can be considered as a pseudo-vector; twice the magnitude of the vector is called *vorticity*. The symmetric tensor:

$$E_{ij} = \frac{1}{2}(\nabla u+(\nabla u)^T) - \frac{\text{trace}[\nabla u]}{N}\delta_{ij} \tag{21}$$

is termed the *rate-of-strain tensor* (or *deformation tensor*) that represents the angular deformation, i.e. the stretching of a fluid element along a principle axis. Notice that in two-dimension cases ($N=2$) Equation 20 corresponds directly to the tensor reparamterization (Equation 7) in which $\gamma_d=\frac{\text{trace}[\nabla u]}{N}$, $\gamma_r=|\Omega_{12}|$, $\gamma_s=\sqrt{E_{11}^2+E_{12}^2}$, and $\theta=\tan^{-1}(\frac{E_{12}}{E_{11}})$. Consider the gradient tensor of a two-dimensional flow field (see Figures 6 and 7 for an example), the counterclockwise and clockwise rotations in the tensor field indicate positive vorticities (red) and negative vorticities (green), respectively . The positive and negative isotropic scalings represent expansion and contraction of the fluid elements (yellow and blue). The anisotropic stretching is equivalent to the rate of angular deformation, i.e., shear strain (white). Furthermore, as illustrated in Figure 3, eigenvectors in the real domain represent deformation patterns of fluid elements, while dual-eigenvectors in the complex domain represent the skewed (elliptical) rotation pattern.

For the analysis of three-dimensional incompressible-fluid flows ($\sum_{i=1}^{3}T_{ii}=0$) confined to a plane (e.g., Figures 6 and 7), twice the trace of ∇u can be written as $T_{11}+T_{22}=-T_{33}$, which represents the net flow to the plane from neighboring

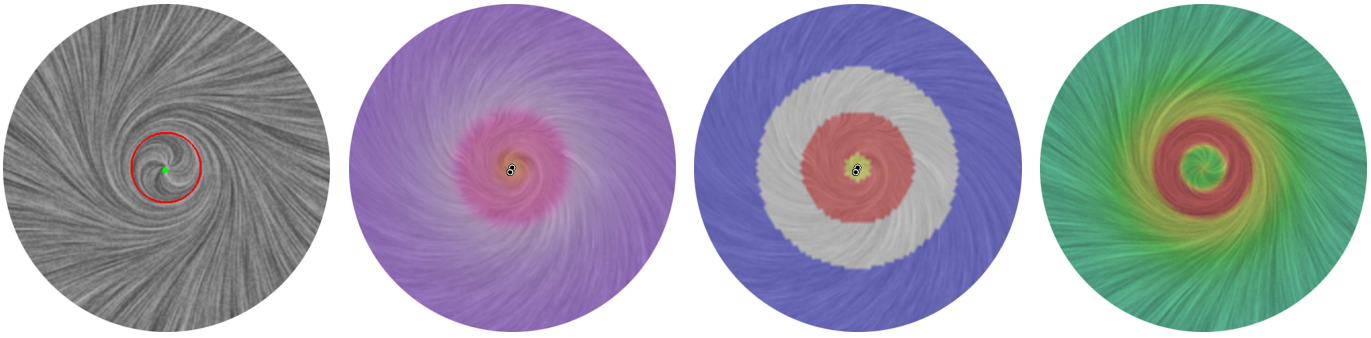

Fig. 9. Four visualization techniques on the Sullivan flow (Section V-A): (a) vector field topology [4] with textures representing the vector field, (b) eigenvalue visualization based on all components with textures showing major eigenvectors in the real domain and major dual-eigenvectors in the complex domain, (c) same as (b) except that colors encode the dominant component, and (d) magnitude (dyadic product) of the velocity gradient tensor with the underlying textures following the vector field. The visualization domain is $r \leq 2.667$.

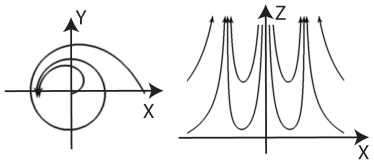

Fig. 8. The Sullivan Vortex viewed in (left) the *x-y* plane and (right) the *x-z* plane.

planes: this is a consequence of mass conservation. Positive scaling in the plane represents the effect of inflow from the 3D neighborhood of the plane. This can be also interpreted as negative stretching of fluid material in the normal direction, i.e. the velocity gradient in the direction normal to the plane is negative ($T_{33} < 0$). A similar interpretation can be made for negative scaling ($T_{33} > 0$). This would be stretching in the normal direction. For compressible fluids, the interpretation requires care: positive scaling can represent not only volumetric dilatation of compressible fluid, but also contain the foregoing effect of inflow of the fluid from the neighborhood of the subject plane.

A. Sullivan Vortex: a Three-Dimensional Flow

The first example we discuss is an analytical 3D incompressible flow that is presented by Sullivan [29]. This is an exact solution of the Navier-Stokes equations for a three-dimensional vortex. The flow is characterized by:

$$u_r(x,y,z)\begin{pmatrix}\cos\theta\\ \sin\theta\\ 0\end{pmatrix}+u_\theta(x,y,z)\begin{pmatrix}-\sin\theta\\ \cos\theta\\ 0\end{pmatrix}+u_z(x,y,z)\begin{pmatrix}0\\ 0\\ 1\end{pmatrix} \tag{22}$$

in which:

$$\begin{aligned} u_r &= -ar+6\nu/r[1-e^{-(ar^2/2\nu)}]\\ u_\theta &= (\Gamma/2\pi r)[H(ar^2/2\nu)/H(\infty)]\\ u_z &= 2az[1-3e^{-ar^2/2\nu}] \end{aligned} \tag{23}$$

are the radial, azimuthal, and axial velocity components, respectively. Here, a (flow strength), Γ (flow circulation), and ν (kinematic viscosity) are constants, $r=\sqrt{x^2+y^2}$, and:

$$H(s)=\int_0^s \exp\{-t+3\int_0^t \frac{1-e^{-\tau}}{\tau}d\tau\}dt \tag{24}$$

Sketches of the flow pattern in the horizontal and vertical planes are shown in Figure 8. Away from the vortex center $r\rightarrow\infty$, the flow is predominantly in the negative radial direction (toward the center) with the accelerating upward flow: $u\approx -ar$, $v\approx 0$, $w\approx 2az$. On the other hand, as r becomes small ($r\rightarrow 0$), we have $u\approx 3ar$, $v\approx 0$, $w\approx -4az$. Figure 9 visualizes one instance of the Sullivan Vortex with $a=1.5$, $\Gamma=25$, and $\nu=0.1$ in the plane $z=1$.

Figure 9 (a) shows the velocity vector field together with the topology [4] identifying the unstable focus (the green dot) and the periodic orbit (the red loop). The images in (b) and (c) are the eigenvalue visualizations based on all components (AC method) and on the dominant component (DC method), respectively. The textures in (b) and (c) illustrate the major eigenvector field in the real domains and the major dual-eigenvector field in the complex domains. Due to the normalization of tensors, our visualization techniques shown in (b) and (c) exhibit relative strengths of tensor components (γ_d, γ_r, and γ_s) at a given point. To examine the absolute strength of velocity gradients in an inhomogeneous flow field, spatial variations of the magnitude (dyadic product) of velocity gradients are provided in (d) with the texture representing the velocity vector field. Red indicate high values and blue correspond to low values.

The behaviors of the third dimension (z-direction) can be inferred from our DC-based eigenvalue visualization in the *x-y* plane (Figure 9 (c)). Namely, in the regions of large r, the negative isotropic scaling (blue) is dominant, and near the vortex center, the positive isotropic scaling (yellow) is dominant. Identifying such isotropic scaling is formidable with the use of texture-based vector visualization (Figure 9 (a)).

The eigenvalue visualization (Figure 9 (b) and (c)) allows us to see stretching-dominated regions (white), which cannot be identified from the corresponding vector field visualization (Figure 9 (a)). Figure 9 (b) and (d) collectively exhibit that strong counterclockwise rotation of fluid parcels appears in the annular region near the center, and the rotation diminishes as r increases (away from the center). Notice that this

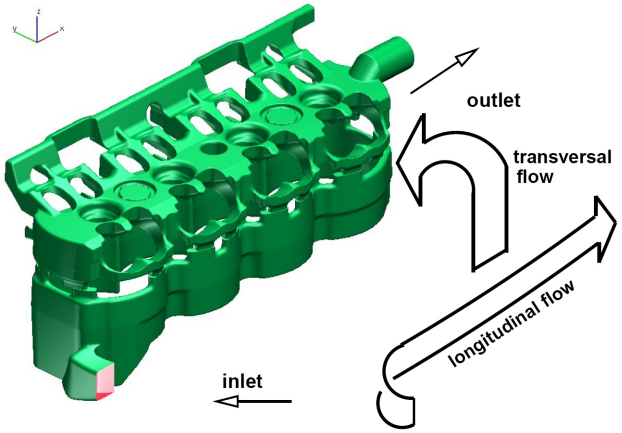

Fig. 10. The major components of the flow through a cooling jacket include a longitudinal component, lengthwise along the geometry and a transversal component in the upward-and-over direction. The inlet and outlet of the cooling jacket are also indicated.

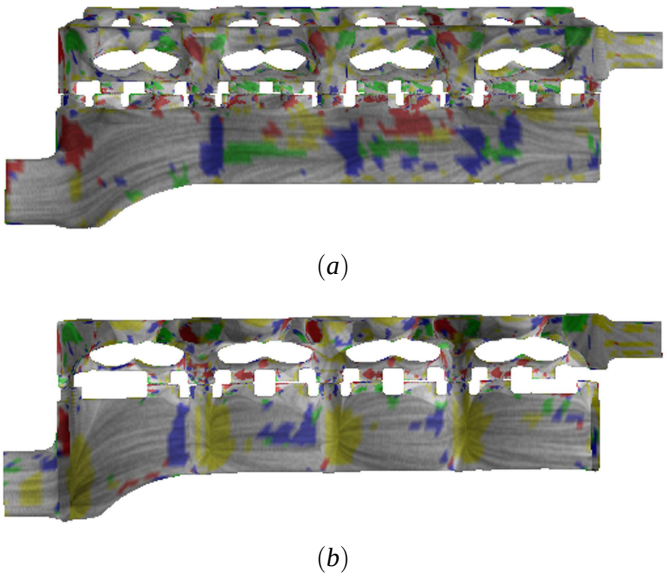

Fig. 11. DC-based eigenvalue visualization of a simulated flow field inside the cooling jacket: (a) the outside surface of a side wall in the cooling jacket, and (b) the inside surface of the same side wall. This is the first time asymmetric tensor analysis is applied to this data set.

information is difficult to extract from the texture-based vector visualization (Figure 9 (a)), although it can be achieved with a vorticity-based visualization.

Comparing the texture plots of Figure 9 (a) and (b), we notice that the major eigenvectors ((b): the directions of stretching) closely align with the streamlines in the real domain (a) for large enough r, while the major dual-eigenvectors ((b): the direction of elongation) are nearly perpendicular to the streamlines (a) in the complex domain near the center of the vortex. This kind of enlightening observations are not revealed without tensor analysis.

The extremely localized high magnitude of velocity gradient (red region) shown in Figure 9 (d) represents the complex flows that resemble the *eye wall* of a hurricane or tornado, although for large r, the Sullivan Vortex differs from hurricane or tornado flows.

To illustrate our visualization techniques earlier in Figures 1, 4, 6, and 7. We have used the combination of two Sullivan Vortices whose centers are slightly displaced with a distance of 0.17 and whose rotations are opposite but of equal strength.

B. Heat Transfer With a Cooling Jacket

A cooling jacket is used to keep an engine from overheating. Primary considerations for its design include 1) achieving an even distribution of flow to each cylinder, 2) minimizing pressure loss between the inlet and outlet, 3) eliminating flow stagnation, and 4) avoiding high-velocity and regions that may cause bubbles or cavitation. Figure 10 shows the geometry of a cooling jacket, which consists of three components: 1) the lower half of the jacket or cylinder block, 2) the upper half of the jacket or cylinder head, and 3) the gaskets to connect the cylinder block to the head. Evidently, the geometry of the surface is highly complex.

In order to achieve efficient heat transfer from the engine block to the fluid flowing in the jacket, the fluid must be continuously convected while being mixed. Consequently, desirable flow patterns to enhance cooling include stretching and scaling that appear on the contact (inner) surface. As discussed earlier, stretching is a measure of fluid mixing. It increases the interfacial area of a lump of fluid material, and the interfacial area is where heat exchange takes place by conduction. Given that the flow in the cooling jacket is considered incompressible [18], scalings that appear on the contact surface, whether positive or negative, indicate the flow components normal to the interface, i.e., convection at the interface. Note that fluid rotations (either counterclockwise or clockwise) would yield inefficient heat transfer at the contact interface since rotating motions do not contribute to the increase of the surface of a lump of fluid material.

This dataset has been examined using various vector field visualization techniques based on velocity and vorticity [22], [18], [19]. We have applied our asymmetric tensor analysis to this data set and discuss the additional insight that has not been observed from previous study.

In order to distinguish the regions of rotation-dominant flows from scalings and anisotropic stretching, we choose to use the DC-based eigenvalue visualization (Figure 11). In (a) and (b), we show the outer and inner surface of the right half of the jacket, respectively. The visualization suggests that the flows are indicative of heat transfer, especially at the inner side of the wall (b). This is because a large portion of the surface area exhibits positive scaling (yellow), negative scaling (blue), and anisotropic and stretching (white), whereas the area of predominantly rotations (red and green) are relatively small. It is emphasized that an important part of the geometry is the inner surface where coolant is directly in contact with engine's cylinders. Comparing the inner and outer surfaces of the cooling jacket provides interesting insights into the flow patterns. In the cylinder blocks between the adjacent cylinders, the flow pattern in the inner surface (b) is divergent (yellow) preceded by convergent flows (blue). The flow path from

one cylinder to another has significant curvature (Figure 10), and a portion of the flow is brought to the upper jacket through the gasket. It appears that curvature-induced advective deceleration and acceleration and the outflow to the upper jacket are responsible for the repetitious flow pattern on the inner surface. On the other hand, the resulting flow contraction is supposed to cause the flow convergence on the outer surface (Figure 11 (a)). Yet, no clear repetitious pattern is present on the outer surface except flow convergence between the cylinders. In general, there is no significant region where flow rotation is dominant on the inner surface. While there are more rotation-dominated regions on the outer surface, it is not as critical as the inner surface. This indicates a positive aspect of the cooling jacket design.

While these flow patterns could be interpreted with vector field visualization, it would require a more careful inspection. On the other hand, our eigenvalue presentation of the tensor field can reveal such characteristics explicitly, automatically, and objectively. For example, to our knowledge, the aforementioned repeating patterns of divergent and convergent flows on the inner surface (Figure 11 (b)) has not been reported from previous visualization work that studies this data set [22], [18], [19].

C. In-Cylinder Flow Inside a Diesel Engine

Swirl motion, an ideal flow pattern strived for in a diesel engine [23], resembles a helix spiral about an imaginary axis aligned with the combustion chamber as illustrated in Figure 12. Achieving this ideal motion results in an optimal mixing of air and fuel and thus a more efficient combustion process. A number of vector field visualization techniques have been applied to a simulated flow inside the diesel engine [23], [11], [4]. These techniques include arrow plots, color coding velocity, textures, streamlines, vector field topology, and tracing particles. We have applied our tensor-based techniques to this dataset, which to our knowledge is the first time asymmetric tensor analysis is applied to this data.

Visualization of both eigenvalues and eigenvectors on the curved surface is presented in Figure 13: (a) AC-based eigenvalue visualization, (b) a hybrid approach with eigenvectors and pseudo-eigenvectors illustrated. We also apply our visualization techniques to a planar vector field obtained from a cross section of the cylinder at 25 percent of the length of the cylinder from the top where the intake ports meet the chamber. The visualization techniques are: (c) AC-based eigenvalue visualization, and (d) DC-based eigenvalue combined with eigenvectors and major dual-eigenvectors. Note that the textures shown in (a) and (c) illustrate the velocity vector field.

Figure 13 (a) and (b) demonstrate that the developed technique for visualizing both eigenvalues and eigenvectors on a *curved* surface. The major eigenvectors in the real domain (stretching direction of fluid parcels) do not align with the streamlines. In some locations, they are perpendicular to each other. On the other hand, the elongation of rotating motion tends to be in the similar direction to the velocity vector (see Figure 3 for the stretching and elongation interpretations in eigenvectors). Note that the trend is opposite to that of the Sullivan Vortex (Figure 9).

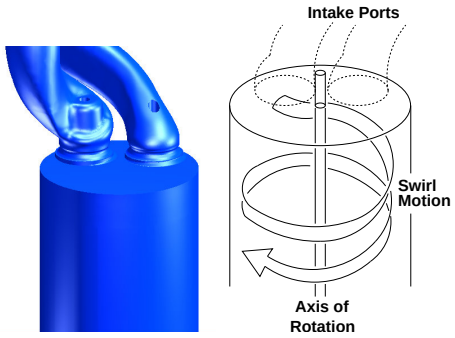

Fig. 12. The swirling motion of flow in the combustion chamber of a diesel engine. *Swirl* is used to describe circulation about the cylinder axis. The intake ports at the top provide the tangential component of the flow necessary for swirl. The data set consists of 776,000 unstructured, adaptive resolution grid cells.

On the cylinder surface shown in (b), there are only two dominant regions: counterclockwise rotation and anisotropic stretching. Lack of regions dominated by isotropic scaling suggests that the flow along the cylinder wall forms no strong flow separation or reattachment, which is consistent with the sketch in Figure 12. On the other hand, the top of the cylinder shows the dominance of negative isotropic scaling, representing that the flow is in the intake cycle. These observations are rather difficult to make from visualization of the velocity vector field, i.e. the texture in Fig 13 (a) alone.

The locations of pure circular rotation of fluid parcels can be spotted in (b) as the degenerating points such as wedges (black dots) and trisectors (white dots). A degenerate point represents the location of zero angular strain. Hence for two-dimensional non-divergent flows, no mixing or energy dissipation can take place at the degenerate points. Nonetheless, it is not exactly the case for three-dimensional and compressible flows in this example, because stretching could still take place in the direction normal to the surface, if isotropic scaling component were present.

The vector plot of Figure 13 (c) shows the complex flow pattern comprising several vortices with both rotations. The complex pattern is resulted from the decelerating flow, since this flow field is taken at the end of the intake process, i.e., the cylinder head is near the bottom end. The overlay of eigenvalues clearly and effectively exhibits the directions of rotation, positive and negative isotropic scaling (expansion and contraction), and anisotropic stretching (shear strain).

In Figure 13 (d), the direction of stretching is readily understood by the major and minor eigenvectors in the real domains and the major dual-eigenvectors in the complex domains. This image also demonstrates the fact, as we demonstrated in Figures 2 and 5, that fluid rotation cannot directly come in contact with the flow of opposite rotational orientation. There must be a region of stretching in-between with the only exception being a pure source or sink. Furthermore, it can be observed that the regions between rotations in the same direction tend to induce stretching. The regions between rotations in the opposite directions tend to generate negative scaling, which

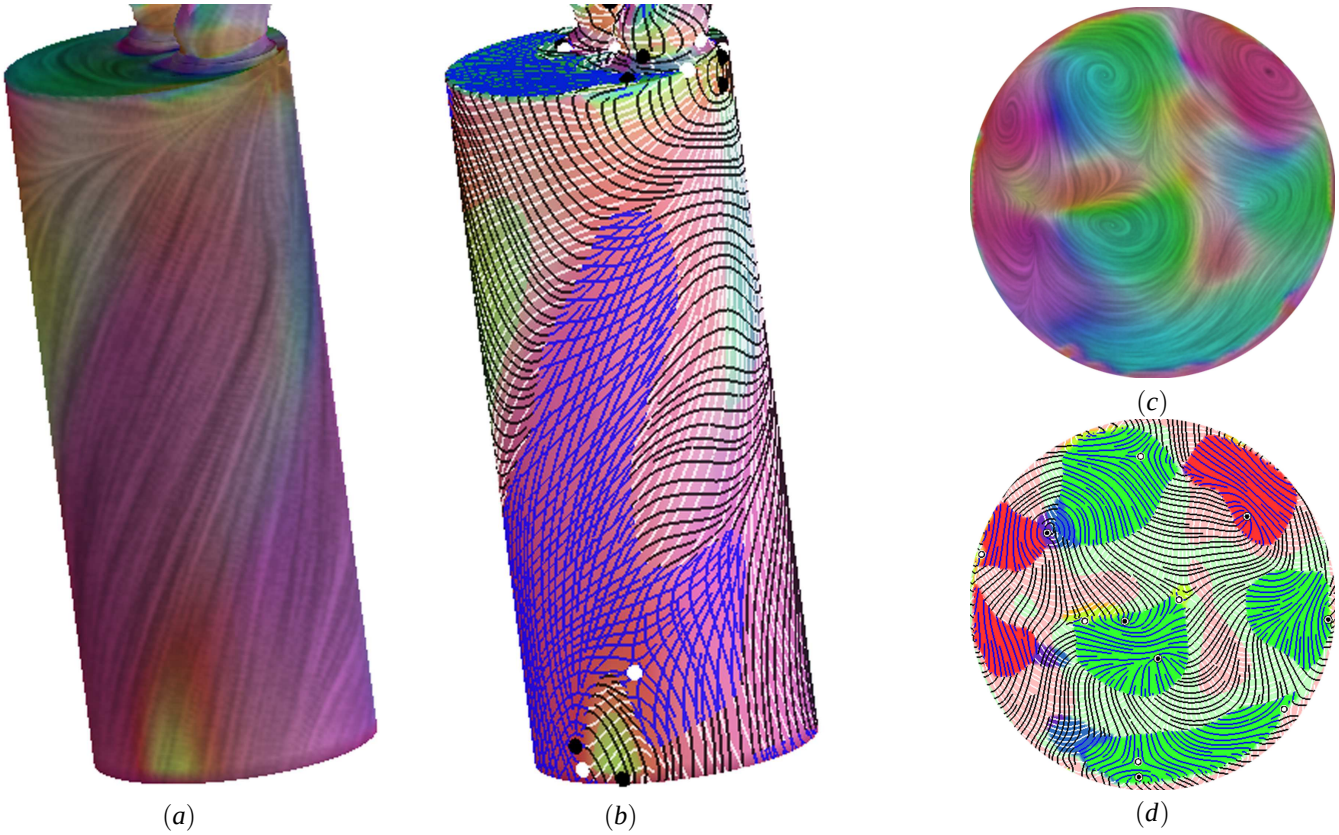

Fig. 13. Visualization of a diesel engine simulation dataset (Section V-C): (a) AC-based eigenvalue visualization of the data on the surface of the engine, (b) hybrid eigenvalue and eigenvector visualization (Figure 7 (b)) of the gradient tensor on the surface with eigenvectors in the real domains and pseudo-eigenvectors in the complex domains, (c) AC-based visualization of a planar slice (cut at 25 percent of the length of the cylinder from the top where the intake ports meet the chamber), and (d) the hybrid visualization used for (b) is applied to the planar slice. The degenerate points are highlighted using colored dots: black for wedges and white for trisectors. This is the first time asymmetric tensor analysis is applied to this set.

represents contraction. There are several degenerate points such as wedges (black dots) and trisectors (white dots) in the figure.

We wish to emphasize that this is the first time the following flow characteristics are visualized for the diesel engine dataset: expansion, contraction, stretching, elongation, and degenerate points. Also, to our knowledge, the observation that the flow along the cylinder wall forms no flow separation or reattachment has not been reported previously based on velocity and vorticity visualizations [23], [11], [4].

VI. Conclusion and Future Work

In this paper, we provide the analysis of asymmetric tensor fields defined on two-dimensional manifolds and develop effective visualization techniques based on such analysis. At the core of our technique is a novel parameterization of the space of 2×2 tensors, which has well-defined physical meanings when the tensors are the gradient of a vector field.

Based on the parameterization, we introduce the concepts of *eigenvalue manifold* (Figure 5) and *eigenvector manifold* (Figure 2) and describe the topology of these objects. For the eigenvalue manifold, we have identified five special modes that lead to a partition of the manifold (Figure 5). Such a partition provides a physically-motivated way of segmenting a tensor field, or a vector field whose gradient is the tensor field of interest.

For the eigenvector field, we augment previous results of Zheng and Pang [39] based on a novel concept of eigenvector manifold (Figure 2). Our analysis includes an explicit characterization of the dual-eigenvectors (Theorem 4.2), a new symmetric discriminant that takes into account the orientation of the rotational component, an algorithm to classify degenerate points (Theorem 4.4) and the extension of the Poincaré-Hopf theorem to asymmetric tensors on two-dimensional manifolds (Theorem 4.5), and the definition of pseudo-eigenvectors (Definition 4.6) which we use to visualize tensor structures inside complex domains.

We present several visualization techniques based on the eigenvalue field, eigenvector field, or their combination. Our analysis and visualization techniques are also adapted to curved mesh surfaces. To the best of our knowledge, this is the first time asymmetric tensor fields on 3D surfaces are analyzed and visualized.

We provide physical interpretation of our approach in the context of flow understanding, which is enabled by the relationship between our tensor parameterization and its physical interpretation. Our visualization techniques can provide a compact and concise presentation of flow kinematics. Principal motions of fluid material consist of angular deformation (i.e. stretching), dilatation (i.e. scaling), rotation, and translation. In our tensor field visualization, the first three components (stretching, scaling, and rotation) are expressed explicitly,

while the translational component is not illustrated. One of the advantages in our tensor visualization is that the kinematics expressed in eigenvalues and eigenvectors can be interpreted physically, for example, to identify the regions of efficient and inefficient mixing. Furthermore, the components of scaling (divergence and convergence) in a two-dimensional surface for incompressible flows can provide information for the three-dimensional flow; negative scaling represents stretching of fluid in the direction normal to the surface, and vice versa.

We demonstrate the efficiency of these visualization methods by applying them to the Sullivan Vortex, an exact solution to the Navier-Stokes equations, as well as two CFD simulation applications for a cooling jacket and a diesel engine.

To summarize, the eigenvalue visualization enables us to examine the relative strengths of fluid expansion (contraction), rotations, and the rate of shear strain in one single plot. Hence such a plot is convenient for inspection of global flow characteristics and behaviors, as well as to detect salient features. In fact, the developed visualization technique should be ideal for the exploratory investigation of complex flow fields. Furthermore, the developed eigenvector visualization allows us to uniquely identify the detailed deformation patterns of fluid parcels, which provides additional insights in understanding of fluid motions. Consequently, the developed tensor-based visualization techniques will provide an additional tool for flow-field investigations.

There are a number of possible future research directions that are promising. First, in this work we have focused on a two-dimensional subset of the full three-dimensional eigenvalue manifold (unit tensors). While this allows an efficient segmentation of the flow based on the dominant component, the tensor magnitude can be used to distinguish between regions of the same dominant component but with significantly different total strengths (Figure 6 (c)). We plan to incorporate the absolute magnitude of the tensor field into our analysis and study the full three-dimensional eigenvalue manifold. Second, tensor field simplification is an important task, and we will explore proper simplification operations and metrics that apply to asymmetric tensor fields. Third, we plan to expand our research into 3D domains as well as time-varying fields.

APPENDIX
PROOFS

In the appendix, we provide the proofs for the theorems from Section IV.

Theorem 4.1: Given two tensors $T_i = T(\theta_i, \varphi)$ $(i = 1,2)$ on the same latitude $-\frac{\pi}{2} < \varphi < \frac{\pi}{2}$, let $N = \begin{pmatrix} \cos\delta & -\sin\delta \\ \sin\delta & \cos\delta \end{pmatrix}$ with $\delta = \frac{\theta_2 - \theta_1}{2}$. Then any eigenvector or dual-eigenvector $\overrightarrow{w_2}$ of T_2 can be written as $N\overrightarrow{w_1}$ where $\overrightarrow{w_1}$ is an eigenvector or dual-eigenvector of T_1, respectively.

Proof: It is straightforward to verify that $T_2 = NT_1N^T$, i.e., T_1 and T_2 are *congruent*. Results from classical linear algebra state that T_1 and T_2 have the same set of eigenvalues. Furthermore, a vector $\overrightarrow{w_1}$ is an eigenvector of T_1 if and only if $\overrightarrow{w_2} = N\overrightarrow{w_1}$ is an eigenvector of T_2.

To verify the relationship between the dual-eigenvectors of T_1 and T_2, let $U_1 \begin{pmatrix} \mu_1 & 0 \\ 0 & \mu_2 \end{pmatrix} V_1$ is the singular value decomposition of T_1. Then $U_2 \begin{pmatrix} \mu_1 & 0 \\ 0 & \mu_2 \end{pmatrix} V_2$ in which $U_2 = U_1N^T$ and $V_2 = NV_1$ is the singular decomposition of T_2. This implies that T_1 and T_2 have the same singular values μ_1 and μ_2.

The relationship between the dual-eigenvectors of T_1 and T_2 can be verified by plugging into Equations 3 and 4 the aforementioned statements on eigenvectors and singular values between congruent matrices. ■

Theorem 4.4: Let T be a continuous asymmetric tensor field defined on a two-dimensional manifold $\mathbf{M}$ satisfying $\gamma_r^2 + \gamma_s^2 > 0$ everywhere in $\mathbf{M}$. Let S_T be the symmetric component of T which has a finite number of degenerate points $K = \{\mathbf{p}_i : 1 \le i \le N\}$. Then we have:

1) K is also the set of degenerate points of T.
2) For any degenerate point $\mathbf{p}_i$, $I(\mathbf{p}_i, T) = I(\mathbf{p}_i, S_T)$. In particular, a wedge remains a wedge, and a trisector remains a trisector.

Proof: Given that $\gamma_s^2(T) + \gamma_r^2(T) > 0$ everywhere in the domain, the degenerate points of T only occur inside complex domains. Recall that the structures of T inside complex domains are defined using the dual-eigenvectors, which are the eigenvectors of symmetric tensor field P_T (Equation 15). Moreover, the set of degenerate points of T is the same as the set of degenerate points of P_T inside complex domains, i.e., $\varphi = \pm\frac{\pi}{2}$.

Notice that the major and minor eigenvectors of P_T are obtained from corresponding eigenvectors of S_T by rotating them either counterclockwise or clockwise by $\frac{\pi}{4}$. Within each connected component in the complex domains, the orientation of the rotation is constant. Zhang et al. [35] show that rotating the eigenvectors of a symmetric tensor field (in this case S_T) uniformly in the domain (in this case a connected component of the complex domains) by an angle of β (in this case $\pm\frac{\pi}{4}$) results in another symmetric tensor field that has the same set of degenerate points as the original field. Moreover, the tensor indices of the degenerate points are maintained by such rotation. Therefore, S_T and P_T (and consequently T) have the same set of degenerate points. Furthermore, the tensor indices are the same between corresponding degenerate points. ■

Theorem 4.5: Let $\mathbf{M}$ be a closed orientable two-dimensional manifold with an Euler characteristic $\chi(\mathbf{M})$, and let T be a continuous asymmetric tensor field with only isolated degenerate points $\{\mathbf{p}_i : 1 \le i \le N\}$. Then:

$$\sum_{i=1}^{N} I(\mathbf{p}_i, T) = \chi(\mathbf{M}) \tag{25}$$

Proof: $\sum_{i=1}^{N} I(\mathbf{p}_i, T) = \sum_{i=1}^{N} I(\mathbf{p}_i, S_T) = \chi(\mathbf{M})$. The first equation is a direct consequence of Theorem 4.4, while the second equation makes use of the fact that S_T is a symmetric tensor field, for which the *Poincaré-Hopf theorem* has been proven true [5]. ■

Theorem 4.7: Given a continuous asymmetric tensor field T defined on a two-dimensional manifold $\mathbf{M}$, let U_1 and U_2 be an α- and β-type region, respectively, where $\alpha, \beta \in \{D^+, D^-, R^+, R^-, S\}$ are different. Then $\partial U_1 \bigcap \partial U_2 = \emptyset$ if α-

and β-types represent regions in the eigenvalue manifold that do not share a common boundary.

Proof: Since ζ_T (Equation 10) is a continuous map from $\mathbf{M}$ to the eigenvalue manifold $\mathbf{M}_\lambda$, we have $\zeta_T^{-1}(\emptyset) = \emptyset$. ■

Theorem 4.8: Given a continuous asymmetric tensor field T defined on a two-dimensional manifold such that $\gamma_d^2 + \gamma_r^2 + \gamma_s^2 > 0$ everywhere, the following are true:

1) an R^+-type region is contained in $W_{c,n}$ and an R^--type region is contained in $W_{c,s}$,
2) an S-type region is contained in $W_{r,n} \bigcup W_{r,s}$,
3) a D^+-type or D^--type region can have a non-empty intersection with any of the following: $W_{r,n}$, $W_{r,s}$, $W_{c,n}$, and $W_{c,s}$.

Proof: Given a point $\mathbf{p}_0$ in an R^+-type region, we have $\gamma_r(\mathbf{p}_0) > \gamma_s(\mathbf{p}_0) \geq 0$, i.e., $\mathbf{p}_0$ is in a complex domain in the northern hemisphere ($W_{c,n}$). Similarly, if $\mathbf{p}_0$ is in an R^--type region, then $\mathbf{p}_0 \in W_{c,s}$.

If $\mathbf{p}_0$ is in an S-type region, then $\gamma_s(\mathbf{p}_0) > |\gamma_r(\mathbf{p}_0)|$, i.e., $\mathbf{p}_0$ is in the real domains that can be in either the northern or the southern hemisphere.

Finally, if $\mathbf{p}_0$ is in a D^+-type region, then $\gamma_d(\mathbf{p}_0) > \max(|\gamma_r(\mathbf{p}_0)|, \gamma_s(\mathbf{p}_0))$. However, there is no constraint on the discriminant $\varphi = \arctan(\frac{\gamma_r}{\gamma_s})$. Therefore, $\mathbf{p}_0$ can be inside any of $W_{r,n}$, $W_{r,s}$, $W_{c,n}$, and $W_{c,s}$. A similar statement can be made when $\mathbf{p}_0$ is in a D^--type region. ■

REFERENCES

[1] P. Alliez, D. Cohen-Steiner, O. Devillers, B. Lévy, and M. Desbrun, "Anisotropic polygonal remeshing," *ACM Transactions on Graphics (SIGGRAPH 2003)*, vol. 22, no. 3, pp. 485–493, Jul. 2003.

[2] G. K. Batchelor, *An Introduction to Fluid Dynamics*. London: Cambridge University Press, 1967.

[3] B. Cabral and L. C. Leedom, "Imaging Vector Fields Using Line Integral Convolution," in *Poceedings of ACM SIGGRAPH 1993*, ser. Annual Conference Series, 1993, pp. 263–272.

[4] G. Chen, K. Mischaikow, R. S. Laramee, P. Pilarczyk, and E. Zhang, "Vector Field Editing and Periodic Orbit Extraction Using Morse Decomposition," *IEEE Transactions on Visualization and Computer Graphics*, vol. 13, no. 4, pp. 769–785, jul–aug 2007.

[5] T. Delmarcelle, "The Visualization of Second-Order Tensor Fields," Ph.D. dissertation, Stanford Applied Physics, 1994.

[6] T. Delmarcelle and L. Hesselink, "Visualizing Second-order Tensor Fields with Hyperstream lines," *IEEE Computer Graphics and Applications*, vol. 13, no. 4, pp. 25–33, Jul. 1993.

[7] T. Delmarcelle and L. Hesselink, "The Topology of Symmetric, Second-Order Tensor Fields," in *Proceedings IEEE Visualization '94*, 1994.

[8] J. Ebling and G. Scheuermann, "Clifford convolution and pattern matching on vector fields," in *Proceedings IEEE Visualization 2003*, 2003, pp. 193–200.

[9] J. Ebling and G. Scheuermann, "Segmentation of Flow Fields Using Pattern Matching," in *Data Visualization, The Joint Eurographics-IEEE VGTC Symposium on Visualization (EuroVis 2006)*, 2006, pp. 147–154.

[10] H. B. Fischer, J. Imberger, E. J. List, R. C. Y. Koh, and N. H. Brooks, *Mixing in Inland and Coastal Waters*. New York: Academic Press, 1979.

[11] C. Garth, R. Laramee, X. Tricoche, J. Schneider, and H. Hagen, "Extraction and Visualization of Swirl and Tumble Motion from Engine Simulation Data," in *Topology-Based Methods in Visualization (Proceedings of Topo-in-Vis 2005)*, ser. Mathematics and Visualization. Springer, 2007, pp. 121–135.

[12] J. L. Helman and L. Hesselink, "Visualizing Vector Field Topology in Fluid Flows," *IEEE Computer Graphics and Applications*, vol. 11, no. 3, pp. 36–46, May 1991.

[13] L. Hesselink, Y. Levy, and Y. Lavin, "The Topology of Symmetric, Second-Order 3D Tensor Fields," *IEEE Transactions on Visualization and Computer Graphics*, vol. 3, no. 1, pp. 1–11, Mar. 1997.

[14] M. Hlawitschka, J. Ebling, and G. Scheuermann, "Convolution and fourier transform of second order tensor fields," *Proceedings of IASTED VIIP 2004*, pp. 78–83, 2004.

[15] H. Hotz, L. Feng, H. Hagen, B. Hamann, K. Joy, and B. Jeremic, "Physically Based Methods for Tensor Field Visualization," in *Proceedings IEEE Visualization 2004*, 2004, pp. 123–130.

[16] J. Jeong and F. Hussain, "On the Identification of a Vortex," *Journal of Fluid Mechanics*, vol. 285, pp. 69–94, 1995.

[17] D. N. Kenwright, "Automatic Detection of Open and Closed Separation and Attachment Lines," in *Proceedings IEEE Visualization '98*, 1998, pp. 151–158.

[18] R. S. Laramee, C. Garth, H. Doleisch, J. Schneider, H. Hauser, and H. Hagen, "Visual Analysis and Exploration of Fluid Flow in a Cooling Jacket," in *Proceedings IEEE Visualization 2005*, 2005, pp. 623–630.

[19] R. S. Laramee, C. Garth, J. Schneider, and H. Hauser, "Texture-Advection on Stream Surfaces: A Novel Hybrid Visualization Applied to CFD Results," in *Data Visualization, The Joint Eurographics-IEEE VGTC Symposium on Visualization (EuroVis 2006)*. Eurographics Association, 2006, pp. 155–162,368.

[20] R. S. Laramee, H. Hauser, H. Doleisch, F. H. Post, B. Vrolijk, and D. Weiskopf, "The State of the Art in Flow Visualization: Dense and Texture-Based Techniques," *Computer Graphics Forum*, vol. 23, no. 2, pp. 203–221, June 2004.

[21] R. S. Laramee, H. Hauser, L. Zhao, and F. H. Post, "Topology Based Flow Visualization: The State of the Art," in *The Topology-Based Methods in Visualization Workshop (TopoInVis 2005), Visualization and Mathematics*, 2007, pp. 1–19.

[22] R. S. Laramee, J. J. van Wijk, B. Jobard, and H. Hauser, "ISA and IBFVS: Image Space Based Visualization of Flow on Surfaces," *IEEE Transactions on Visualization and Computer Graphics*, vol. 10, no. 6, pp. 637–648, Nov. 2004.

[23] R. S. Laramee, D. Weiskopf, J. Schneider, and H. Hauser, "Investigating Swirl and Tumble Flow with a Comparison of Visualization Techniques," in *Proceedings IEEE Visualization 2004*, 2004, pp. 51–58.

[24] J. M. Ottino, *The kinematics of mixing: stretching, chaos and transport*. Cambridge, MA: Cambridge University Press, 1989.

[25] R. Peikert and M. Roth, "The Parallel Vectors Operator - A Vector Field Visualization Primitive," in *Proceedings of IEEE Visualization '99*. IEEE Computer Society, 1999, pp. 263–270.

[26] I. A. Sadarjoen and F. H. Post, "Detection, Quantification, and Tracking of Vortices using Streamline Geometry," *Computers and Graphics*, vol. 24(3), pp. 333–341, June 2000.

[27] F. Sherman, *Viscous flow*. New York: McGraw-Hill, 1990.

[28] D. Sujudi and R. Haimes, "Identification of Swirling Flow in 3D Vector Fields," American Institute of Aeronautics and Astronautics, Tech. Rep. AIAA Paper 95–1715, 1995.

[29] R. D. Sullivan, "A two-cell vortex solution of the navier-stokes equations," *Journal of Aero/Space Sciences*, vol. 26, no. 11, pp. 767–768, Nov. 1959.

[30] X. Tricoche, G. Scheuermann, and H. Hagen, "Tensor Topology Tracking: A Visualization Method for Time-Dependent 2D Symmetric Tensor Fields," in *Computer Graphics Forum 20(3) (Eurographics 2001)*, Sep. 2001, pp. 461–470.

[31] X. Tricoche, G. Scheuermann, and H. Hagen, *Topology Simplification of Symmetric, Second-Order 2D Tensor Fields, Hierarchical and Geometrical Methods in Scientific Visualization*. Springer, 2003.

[32] X. Tricoche, G. Scheuermann, H. Hagen, and S. Clauss, "Vector and Tensor Field Topology Simplification on Irregular Grids," in *Proceedings of the Joint Eurographics - IEEE TCVG Symposium on Visualization (VisSym-01)*. Springer-Verlag, May 28–30 2001, pp. 107–116.

[33] J. J. van Wijk, "Image Based Flow Visualization," *ACM Transactions on Graphics*, vol. 21, no. 3, pp. 745–754, 2002.

[34] C. Ware, *Information Visualization: Perception for Design, Second Edition*. Morgan Kaufmann, 2004.

[35] E. Zhang, J. Hays, and G. Turk, "Interactive tensor field design and visualization on surfaces," *IEEE Transactions on Visualization and Computer Graphics*, vol. 13, no. 1, pp. 94–107, 2007.

[36] E. Zhang, K. Mischaikow, and G. Turk, "Vector field design on surfaces," *ACM Transactions on Graphics*, vol. 25, no. 4, pp. 1294–1326, 2006.

[37] X. Zheng and A. Pang, "Hyperlic," *Proceeding IEEE Visualization*, pp. 249–256, 2003.

[38] X. Zheng and A. Pang, "Topological Lines in 3D Tensor Fields," in *Proceedings IEEE Visualization '04*, 2004, pp. 313–320.

[39] X. Zheng and A. Pang, "2D Asymmetric Tensor Fields," in *Proceedings IEEE Visualization 2005*, 2005, pp. 3–10.

[40] X. Zheng, B. Parlett, and A. Pang, "Topological Structures of 3D Tensor Fields," in *Proceedings IEEE Visualization 2005*, 2005, pp. 551–558.